



UNIVERSITY OF LEEDS

This is a repository copy of *Universal synthesis method for mixed phase TiO₂(B)/anatase TiO₂ thin films on substrates via a modified low pressure chemical vapour deposition (LPCVD) route.*

White Rose Research Online URL for this paper:
<http://eprints.whiterose.ac.uk/97147/>

Version: Accepted Version

Article:

Chimupala, Y, Junploy, P, Hardcastle, T et al. (4 more authors) (2016) Universal synthesis method for mixed phase TiO₂(B)/anatase TiO₂ thin films on substrates via a modified low pressure chemical vapour deposition (LPCVD) route. *Journal of Materials Chemistry A*, 4 (15). pp. 5685-5699. ISSN 2050-7488

<https://doi.org/10.1039/C6TA01383J>

Reuse

Unless indicated otherwise, fulltext items are protected by copyright with all rights reserved. The copyright exception in section 29 of the Copyright, Designs and Patents Act 1988 allows the making of a single copy solely for the purpose of non-commercial research or private study within the limits of fair dealing. The publisher or other rights-holder may allow further reproduction and re-use of this version - refer to the White Rose Research Online record for this item. Where records identify the publisher as the copyright holder, users can verify any specific terms of use on the publisher's website.

Takedown

If you consider content in White Rose Research Online to be in breach of UK law, please notify us by emailing eprints@whiterose.ac.uk including the URL of the record and the reason for the withdrawal request.



eprints@whiterose.ac.uk
<https://eprints.whiterose.ac.uk/>

Universal synthesis method for mixed phase TiO₂(B)/anatase TiO₂ thin films on substrates via a modified low pressure chemical vapour deposition (LPCVD) route

Yothin Chimupala^{a,d}, Patcharanan Junploy^{b,a}, Trevor Hardcastle^a, Aidan Westwood^a, Andrew Scott^a, Benjamin Johnson^c and Rik Brydson^{*a}

^a Institute for Materials Research, School of Chemical and Process Engineering, University of Leeds, Leeds, LS2 9JT, UK. Email: R.M.Drummond-Brydson@leeds.ac.uk

^b Department of Chemistry, Faculty of Science, Chiang Mai University, Chiang Mai, 50200, Thailand

^c School of Physics and Astronomy, University of Leeds, Leeds, LS2 9JT, UK

^d Department of Industrial Chemistry, Faculty of Science, Chiang Mai University, Chiang Mai, 50200, Thailand

Abstract

A universal method for the synthesis of mixed phase TiO₂ Bronze(B)/ anatase titania thin films by Low Pressure Chemical Vapour Deposition (LPCVD) onto any substrate is presented. General LPCVD conditions were titanium isopropoxide (TTIP) and N₂ gas as the precursor and carrier gas respectively, 600°C nominal reaction temperature, and 15 min reaction time; a range of different substrates were investigated including: a silicon wafer, fused quartz, highly ordered pyrolytic graphite (HOPG) and pressed graphite flake (graffoil). X-ray diffraction, Raman spectroscopy, X-ray Photoelectron spectroscopy, scanning and transmission electron microscopy were used to characterise the thin films which exhibited a columnar morphology together with smaller equi-axed particles. Pre-treatment of substrates by spraying with a Na-containing solution was found to encourage the crystallization of TiO₂(B) during the LPCVD process. Increasing the concentration of Na in the pre-treatment process resulted in a higher proportion of TiO₂(B) in the thin films up to an optimum condition of 0.75% w/v of Na. Na diffusion from the substrate surface into the adjacent TiO₂ is the proposed mechanism for promoting TiO₂(B) formation as opposed to the anatase phase with Density Functional Theory (DFT) modelling suggesting the presence of Na stabilises the TiO₂(B) phase. Dye degradation tests indicate an increased photocatalytic activity for mixed phase anatase/TiO₂(B) thin films.

Introduction

Titanium dioxide (TiO₂) is a very versatile material utilised in many fields of application: as a photocatalyst,¹ a photovoltaic,² an ubiquitous white pigment³ and as an optically reflective coating.⁴ Additionally, TiO₂ has recently been proposed as an electrode material for lithiation in lithium-ion batteries owing to its cost effectiveness, environmental friendliness and structural stability over multiple charge/discharge cycles.⁵⁻⁹ Many polymorphs of TiO₂ such as anatase, rutile, brookite and bronze (B) phases, as well as metal titanates such as Li₄Ti₅O₁₂, have been reported as effective anode materials for Li ion batteries.^{7,10-12}

Amongst the titania polymorphs, the TiO₂(B) or bronze phase attracts increasing interest due to its monoclinic structure with a low-density crystal framework and larger channels and pores as compared with the other titania polymorphs (anatase, rutile and brookite) as shown in figure 1.¹⁰ Mixed phase TiO₂(B)/anatase has been reported to exhibit higher photocatalytic activity than pure anatase^{10,13-15}. Furthermore, the pores in TiO₂(B) potentially allow intercalation of Li into the structure and result in nanoparticulate TiO₂(B) having an optimum theoretical charge capacity of around 335 mAh/g, which is higher than for titanates such as Li₄Ti₅O₁₂ (175 mAh/g) and would be satisfactory for Li-ion battery applications when compared with a typical commercial graphite electrode (372 mAh/g). The presence of such pores in TiO₂(B) anode materials leads to only a minor volume expansion during Li intercalation (~10% of the volume expansion observed in graphite electrodes), resulting in low levels of generated heat. In addition, graphite is sensitive towards electrolytes and can easily be exfoliated, limiting its utilization.¹⁶⁻¹⁹

Two-dimensional (2D) thin films are often used as electrodes in nano/micro batteries. The crucial factors governing the performance of a 2D electrode include the energy density or areal capacity (mAh/cm²) which directly depends on film thickness and surface area. Reducing 2D film thickness may increase the power density because of the shorter diffusion distance for Li ions, thus nanostructuring can improve the electrochemical activity of TiO₂-based electrodes leading to enhanced cycle life, charge/discharge rate and charge capacity.²⁰⁻²²

2D electrodes based on TiO₂ have been directly deposited as films of nanometre thickness on conductive materials by a number of techniques including sputtering,^{23,24} physical deposition,²⁵ pulsed laser deposition²⁶ and chemical vapour deposition (CVD).^{27,28} However, it is difficult to form the potentially promising TiO₂(B) phase. Low Pressure CVD (LPCVD) is a low-cost process involving relatively non-complicated fabrication systems which can be easily adapted for industrial scale production. In a previous publication, we reported the formation of mixed phase TiO₂(B)/anatase thin films containing a majority of the TiO₂(B) phase using low pressure chemical vapour deposition (LPCVD) at 600°C on soda-lime glass substrates.²⁹ It was found that TiO₂(B) formed as a result of diffusion of Na from the soda-lime glass substrate which encouraged phase formation during the deposition process. This

finding is promising as it may lead to LPCVD being selected for the synthesis of TiO₂(B) thin films providing they can be deposited on conducting substrates for application in Li ion battery anodes.

To address this issue, we propose a new method involving pre-treatment of substrates with Na derived from external sources prior to LPCVD deposition, in order to promote TiO₂(B) formation as a result of Na diffusion from this pre-treated surface layer. We demonstrate the success of this approach using Si wafer, fused quartz, HOPG and grafoil substrates.

The robustness of the method across different substrates alludes to the important role played by Na in facilitating TiO₂(B) growth, potentially opening new routes to TiO₂(B) nanostructuring. This notion is complemented with first-principles calculations which reveal the favourable energetic consequences of Na interstitials in TiO₂(B). TiO₂(B) has already been quite extensively studied from a purely theoretical perspective including its bulk properties,^{30,31} surface chemistry^{32,33} and especially the energetic and structural considerations relating to Li intercalation in the last few years.³⁴⁻⁴¹ These Li intercalation studies serve as a useful benchmark for the calculations presented here. For broader perspective, a comprehensive review of theoretical studies of less common TiO₂ phases has been published by De Angelis et al.⁴²

Experimental Procedure

Substrate Pre-treatment

The substrates used were: <100> oriented silicon wafer, fused quartz, highly ordered pyrolytic graphite (HOPG) and grafoil (pressed, pure natural graphite flake). These were cut into dimensions of 11 mm x 11 mm x 1.0 mm (thickness). The substrates were initially cleaned by sonication in ethanol and then pre-treated by spraying onto the surface 0.5 mL of a sodium-containing solution, i.e. sodium ethoxide (NaOEt) dissolved in Ethanol (99.00%) in varying concentrations between 0.0-5.0 %^{w/v} of Na. Following investigation, the distance between the substrate surface and the spray nozzle was fixed at 15 cm and after spraying, the Na-coated substrates were slowly dried in air at 50°C for 12 hr.

TiO₂ Thin Film Deposition

Low pressure chemical vapour deposition (LPCVD) was used to prepare TiO₂ thin films on the desired pre-treated substrate; details of this equipment being described in a previous publication.²⁹ From our previous studies, the optimum conditions for the synthesis of the TiO₂(B) phase on soda-lime glass substrates was 600°C at a pressure of 25 mbar and hence the same conditions were applied here. The CVD precursor was 5 mL of Titanium tetra-isopropoxide (TTIP, 97%) which was loaded into a pre-set bubbling chamber at 90-95°C in a silicone oil bath. The tube reactor was pre-heated at 600°C before opening the valve to allow the TTIP vapour to be carried into the reaction chamber by N₂ gas at a flow rate of 1 L/min. TiO₂ was deposited onto the target substrate for 15 min then the N₂ gas cylinder valve was closed and the system allowed to cool down to room temperature. Sample nomenclature was x%_Substrate, where x and Substrate are the %^{w/v} of the sprayed Na solution and type of substrate respectively

Materials Characterization

X-ray diffraction (XRD) and Raman spectroscopy were used to investigate the phases present in the thin films. XRD was undertaken using a Philips X'Pert MPD diffractometer using Cu K α X-ray radiation. Raman spectroscopy was conducted on a Renishaw inVia Raman microscope with a green laser of wavelength 514 nm and laser power of 25 mW, scanning a wavenumber range of 3200-100 cm⁻¹. The surface morphologies and thicknesses of the films were examined by scanning electron microscopy (SEM, Hitachi SU8230 Cold-field emission SEM) and energy dispersive X-ray (EDX) analysis (Oxford Instruments) both in plan-view and also in cross-section following fracture. For preparing transmission electron microscopy (TEM) samples, either the synthesised thin films were simply scraped off their substrates with a scalpel, dispersed in isopropyl alcohol and drop cast onto holey carbon supports on copper TEM grids, or Focused Ion Beam (FIB, FEI Nova 200) milling was used to prepare thin cross-sectional lamellae. TEM Specimens were examined using bright field, dark field and phase contrast imaging, selected area electron diffraction (SAED) and EDX spectroscopy, mapping and quantification (Oxford Instruments AZTEC) at 200 kV using a FEI Tecnai G2 TEM/STEM. For X-ray photoelectron spectroscopy (XPS), the thin film sample was analysed using a Thermo EscaLab 250, with an Al K α monochromated X-ray source. A spot size of 500 μ m was used for the analysis. Initially an overall survey scan (1250-0 eV) using a pass energy of 150 eV, a dwell time of 50 ms and step size of 1 eV was taken, followed by detailed scans of the main peaks for the elements identified, using a pass energy of 20 eV, dwell time of 50 ms and step size of 0.1 eV. Depth profiling was conducted using an EX05 Argon ion source, calibrated to a sample current of 1 μ A, over an etch area of 3x3 mm². The measured data was fitted using Casa XPS (Casa Software Ltd, UK), using relative sensitivity factors based upon the scheme where C1s = 1.

Photocatalytic Degradation of Methylene Blue

The basic photocatalytic activities of the TiO₂ thin films were measured in terms of the degradation of methylene blue. An experiment was performed using 25 mm² slides of the prepared titania thin film samples (corresponding to a mass of TiO₂ of 0.0010 g) as the photocatalyst which was placed on the bottom of a 15 mL cylindrical Pyrex vessel. The vessels were filled with 5 mL of the initial methylene blue concentration (*C*₀) of 4×10⁻⁶ M in de-ionised water. Four 18 W tubular black light lamps which emit UV-light in the region 315-400 nm (UV-A) were used as the UV-light source. After keeping the reaction vessels in a dark box for 30 min, the vessels were irradiated with UV-light for 6 hours and the degraded methylene blue solution was then transferred to UV-Quartz cuvette to measure the degradation by UV-Vis spectroscopy (Lambda 25 Perkin Elmer) using the absorbance intensity at 664 nm. Evolved CO₂ was not monitored during the photocatalytic reaction.

Theoretical calculations

To investigate the effects of Na on the stability of TiO₂(B) and anatase at the atomic scale, theoretical density functional theory^{43,44} (DFT) calculations were carried out using the plane wave code CASTEP.^{45†} It is well known^{32,46-48} that DFT fails to predict the experimentally-confirmed⁴⁹ energetic ordering of TiO₂ phases for the most commonly used exchange-correlation (XC) functionals. DFT calculations currently cannot, therefore, be used to reliably compare the stabilities of different TiO₂ phases. However, it is certainly possible to make valid predictions of how defects such as interstitials can change the stability of a given TiO₂ phase in its own right, and that is done in this work. We focus primarily on the case of Na interstitials in TiO₂(B) and anatase, with the additional case of Ti interstitials in TiO₂(B) as a comparison. The stability of ionic crystals is conventionally understood in terms of the formation energy *E*_{for} and/or cohesive energy *E*_{coh}. Either of these two energies is suitable for studying changes to TiO₂ crystal stability due to Na enrichment, so the formation energy *E*_{for} was calculated as the standard enthalpy of formation at zero temperature using

$$E_{for} = E_{Ti_nO_{2n}Na_m(supercell)} - mE_{Na(bcc)} - nE_{Ti(hcp)} - 2n\left(\frac{1}{2}E_{O_2(gas)}\right)$$

where *E*_{Ti(hcp)} and *E*_{Na(bcc)} are the energies per atom in fully optimised bulk Ti and Na metal respectively and *E*(O_{2(gas)}) is the energy of a single optimised O₂ molecule in a large supercell. (*E*_{coh} can be found similarly by calculating the energy of a single atom of each of the constituent elements.)

With some testing, it was found that the exchange-correlation functional of Perdew, Burke and Ernzerhof (PBE)⁵⁰ and the LDA combined with the van der Waals correction scheme of Ortmann, Bechstedt and Schmidt (LDA+OBS),⁵¹ disagree with each other on which of anatase and B phase is most stable. Thus, to make it especially clear that our calculations are meaningful, both of these functionals were used to calculate formation energies in order to demonstrate the consistency of the results. We focus in particular on the changes to *E*_{for} with increasing Na concentration for the TiO₂(B) and anatase phases (and Ti in B phase) by performing structural relaxations on volume-relaxed supercells with and without Na interstitials in the voids, i.e. with *m* = 0 and *m* > 0 as appropriate. Due to the varying ratios of Na:TiO₂ across the different supercells used, it was decided that normalising the energies by supercell volume was more meaningful than normalising by atom numbers or by moles of TiO₂. It was also found that the total energies of supercells of fixed chemical formula but varying configurations (i.e. placing *m* Na atoms in *v* voids where *v* > *m*) were quite insensitive to the choice of configuration; an especially fortunate finding considering the scaling properties of sums of binomial coefficients with increasing *v*. Computational details are provided in an extended footnote.

Energy barriers for migration of Na interstitials between voids within TiO₂(B), denoted Δ*E*, were also calculated using the PBE functional along the three directions [100], [010] and [001] as illustrated in Figure 2, to try to shed some light on the growth conditions. Reaction endpoints were nominated by fully relaxing Ti₄₈O₉₆Na supercells with Na interstitials in adjacent voids, and the energy saddle points associated with the intermediate transition states were then found to within a forces tolerance of 0.05 eVÅ⁻¹ using the quadratic synchronous transit (QST) scheme⁵² implemented for systems under periodic boundary conditions.⁵³

Results

X-ray Diffraction

In a control experiment without Na pre-treatment, XRD (figure 3) reveals the presence of only anatase in the thin films. The XRD patterns of the films on the 4 different substrates following Na pre-treatment are also shown in figure 3. XRD of the 0.5%_Si and 0.5%_Fused quartz samples clearly show peaks which can be assigned to TiO₂(B) (JCPDS 04-007-6246) and anatase (JCPDS 00-021-1272) phases together with peaks from the Si wafer substrate (labelled S) and a broad peak lying between 20-23° 2θ from the amorphous quartz substrate respectively. Although it is difficult to be quantitative owing to the rather uncontrolled nature of the pre-treatment spraying process, it would appear the relative proportion of TiO₂(B) on the fused quartz substrate is reduced relative to the silicon substrate which could be due to the increased diffusion of Na ions into fused quartz relative to silicon. Calculated crystallite (grain) sizes of the TiO₂(B) and anatase phases derived using XRD line broadening and Scherrer's equation are 42±5 and 30±5 nm

respectively on 0.5%_Si, while for 0.5%_Fused quartz the corresponding values are 40 ± 5 nm and 35 ± 5 nm. However, for both the 0.5%_HOPG and 0.5%_Grafoil samples only intense peaks at 26.48° and 54.57° are observed corresponding to the (002) and (004) spacings of the highly oriented graphite substrates (JCPDS 00-041-1487), with no obvious diffraction peaks of TiO₂(B) or anatase evident; this was the case even if the substrate was oriented slightly off axis. The latter method was used to study the lower loadings of Na in the (Si) substrate pre-treatment process (see later - figures 15 and 16), which showed that Na loadings $\geq 0.16\%$ w/v were necessary to promote TiO₂(B) phase formation.

Raman Spectroscopy

Owing to the sensitivity issue with XRD when in the presence of a highly oriented substrate, the thin films on all four substrates were also characterized by Raman spectroscopy and the results are displayed in figure 4. For the control experiment (0.0%_Si) as well as for low Na pre-treatment loadings (0.1%_Si), only evidence for anatase was found in agreement with XRD. It may be seen that Raman active modes of both TiO₂(B) and anatase phases are present in all other samples (with loadings of 0.5% w/v Na), in addition to the characteristic peaks from the substrates which are 520.80 cm^{-1} for the Si wafer and 1584.71 cm^{-1} for graphitic substrates (both HOPG and Grafoil).⁵⁴ The Raman active modes for anatase appear as an intense peak at 141.53 cm^{-1} with three other weaker peaks at 399.60 , 512.31 and 631.98 cm^{-1} ,⁵⁵ whereas the remaining peaks are all Raman active modes of the TiO₂(B) phase, particularly three strong peaks at 122.05 , 196.21 and 361.76 cm^{-1} .³⁰ However, the relative intensities of the anatase and TiO₂(B) Raman peaks cannot be compared directly in order to determine phase fractions, as the relative sensitivity of the anatase-active modes is six times higher than those of the TiO₂(B) phase.^{56,57} Nonetheless, the Raman results do confirm that all thin film samples with Na pre-treatment of 0.5% w/v Na consist of a mixed phase of TiO₂(B) plus anatase.

Scanning Electron Microscopy

SEM plan view images of 0.5%_Si, 0.5%_Fused quartz, 0.5%_HOPG and 0.5%_Grafoil samples are shown in figure 5. These all show similar particle morphologies consisting of a majority of equi-axed/spherical primary particles (possibly single crystallites) of around 20-50 nm which appear aggregated, together with a minor component of larger particles with an irregular polygonal-like appearance. From this bimodal distribution, the average primary particle sizes in 0.5%_Si, 0.5%_Fused quartz, 0.5%_HOPG and 0.5%_Grafoil are 56.3 ± 1.2 (S.D=19.8), 49.7 ± 1.2 (S.D=18.6), 44.1 ± 1.2 (S.D=15.7) and 91.7 ± 1.2 (S.D=64.4) nm respectively. All samples show similar particle sizes except 0.5%_Grafoil which is almost two times as large, as seen in figure 5(d).

BET surface area measurement using nitrogen adsorption gave low surface areas for all samples. Consequently approximate (areal) % porosities of the TiO₂ thin films were determined via plan-view image analysis (ImageJ software) of the SEM images in figure 5. Porosities are given in Table 1 and all samples exhibited similar values, except for 0.5%_Si % which appeared to be slightly more porous.

SEM/EDX was also used to investigate the thin film compositions and the results are given in Table 1. As the electron beam interaction volume penetrates below the thin films, the exact compositions are dependent not only on the type of substrate but also the thickness of the TiO₂ films. However, the results confirm the presence of a titanium oxide thin film with retention of sodium in the deposited structure.

In figure 6, cross-sectional samples have been investigated by SEM and reveal the thickness and physical morphology of the TiO₂ films. The average thicknesses of the TiO₂ layers in 0.5%_Si, 0.5%_Fused quartz and 0.5%_HOPG are all approximately 0.5 μm as shown in table 1. Interestingly, in 0.5%_Grafoil the film is found to be significantly thicker at around 2.1 μm , which is strange as all deposition parameters (such as substrate position in furnace tube relative to the gas entry point, the quantity of TTIP precursor, the carrier gas flow rate, the reaction temperature and reaction time) were carefully controlled and remained constant. It may be that the increased surface roughness of the Grafoil may have caused the as-deposited films to become thicker.⁵⁸ Cross-sectional SEM images of 0.5%_Si, 0.5%_Fused quartz and 0.5%_HOPG, all show columnar growth of TiO₂ nanoparticles with a minority of smaller, rounder nanoparticles predominantly present at the substrate interface. In contrast 0.5%_Grafoil (figure 6(d)) exhibits irregularly-shaped larger particles.

Transmission Electron Microscopy

Figure 7 shows the TEM results from sample 0.5%_Si and reveals an equi-axed grain morphology with a grain-size range of 20-80 nm and an average of ca. 35 nm. The inset magnified image in figure 7(a), exhibits a lattice fringe spacing of $5.86\pm 0.02\text{ \AA}$ consistent with the (200) spacing of TiO₂(B). Further, the HRTEM image in figure 7(b) shows lattice fringes of spacing $3.57\pm 0.02\text{ \AA}$ which can be indexed as the (110) lattice spacing of TiO₂(B) whilst a Fast Fourier Transform (FFT) of the area defined by the red square in figure 7(b) indexes to the TiO₂(B) phase. Conversely, figure 7(c) provides evidence for lattice spacings of anatase TiO₂: $3.47\pm 0.02\text{ \AA}$, $2.41\pm 0.02\text{ \AA}$ and $2.32\pm 0.02\text{ \AA}$ corresponding to the (101), (103) and (004) interplanar spacings respectively. An FFT of the area defined by the red square in figure 7(c) indexes to TiO₂ anatase.

A bright-field TEM image of sample 0.5%_Fused Quartz is shown in figure 8(a) and again shows an equi-axed grain morphology with a grain size of between 20 and 80 nm. The lattice spacing of $3.47\pm 0.02\text{ \AA}$ assigned as (101) of anatase is illustrated in the inset image in figure 8(a). As displayed in figure 8(b), TiO₂(B) lattice spacings were also found to be present in other grains. Furthermore, TEM selected area diffraction from a group of grains is shown in figure 8(c) and reveals ring spacings characteristic of both TiO₂(B) (the (200), (110), (400), (401), (113), (020), (113) and (022) spacings) and also anatase (the (101), (112), (004), (200), (105) and (211) spacings). We observed that anatase and TiO₂(B) phases possessed a similar grain size and grain morphology.

A typical low-magnification TEM image of sample 0.5%_HOPG is shown in figure 9(a), suggesting a smaller grain size of between 20-60 nm than for samples 0.5%_Si and 0.5%_Fused quartz. A TEM image of a grain together with a selected area diffraction pattern is displayed in figure 9(b), the lattice spacings of $3.60\pm 0.02 \text{ \AA}$ and $5.87\pm 0.02 \text{ \AA}$ with an interplanar angle of 73° are consistent with the (110) and (200) spacings of $\text{TiO}_2(\text{B})$, whilst the diffraction pattern also indexes to $\text{TiO}_2(\text{B})$. In figure 9(c), selected area electron diffraction from a group of grains exhibits rings corresponding to the (200), (110), (002), (111), (400), (401) and (003) lattice spacings of $\text{TiO}_2(\text{B})$, as well as the (101), (103) and (004) lattice spacings of the anatase phase and also reveals the coexistence of both phases in this sample.

A range of titanium dioxide grains in the 0.5%_Grafoil sample is presented in a typical TEM image with an inset image in figure 10(a); the grains range in size between 20-100 nm which is bigger than for the other LPCVD samples and correlates with the SEM image shown in figure 5(d). A high resolution TEM image of a group of titania grains with a corresponding fast Fourier transform from the area defined by the red square in figure 10(b), indicates the $\text{TiO}_2(\text{B})$ phase. Finally, a selected area electron diffraction pattern from a number of grains is shown in figure 10(c) and exhibits polycrystalline $\text{TiO}_2(\text{B})$ and anatase ring spacings.

TEM results confirm the presence of both anatase and $\text{TiO}_2(\text{B})$ phases in all samples, in agreement with the findings of Raman and XRD. However in order to investigate the microstructure of the film in more detail, a TEM cross-section was prepared by the Focused Ion Beam (FIB) lift-out method. Bright field TEM images of a cross-sectional sample of 0.5%_Si sample are shown in figure 11(a) and reveal a columnar morphology with crystal growth perpendicular to the Si wafer substrate. Closer inspection at the interface between the substrate and the titania film reveals smaller more equi-axed grains as observed by SEM (figure 6a). Two high resolution TEM images are presented in figures 11(b) and 11(c) which are taken from two different regions within the titania thin film: figure 11(b) is an interfacial region between the Si wafer substrate and the TiO_2 film, whilst figure 11(c) is an area of thin film near the top surface which is close to the protective Pt layer deposited in the FIB. The small grains at the interface in figure 11(b), exhibit lattice spacings of $6.11\pm 0.06 \text{ \AA}$ and $5.78\pm 0.06 \text{ \AA}$ which are assigned to the (001) and (200) planes of $\text{TiO}_2(\text{B})$ respectively. A larger particle at the top surface (figure 11(c)) shows a lattice spacing of $6.20\pm 0.06 \text{ \AA}$ corresponding to (001) $\text{TiO}_2(\text{B})$. Thus it would appear that $\text{TiO}_2(\text{B})$ is formed throughout the film, in contrast to our previous studies of mixed phase anatase/ $\text{TiO}_2(\text{B})$ thin films produced by LPCVD on low sodium content materials such as soda-lime glass,²⁹ where we observed the $\text{TiO}_2(\text{B})$ phase only at interface with the substrate.

Scanning Transmission Electron Microscopy (STEM) and EDX spectroscopy on the FIB cross-sectional 0.5%_Si sample, was used to study the elemental distributions in the thin film. Figure 12 shows the element-specific maps obtained and reveal a relatively uniform distribution of Na throughout the whole TiO_2 thin film, although there is some suggestion of a relative increase in Na concentration at the TiO_2/Si wafer interface. This is confirmed by more detailed STEM/EDX linescans that are shown in figure 13. Note, due to the overlap between the Na K- and Ga L α - X-ray emission lines, elemental quantification in the upper portion of the TiO_2 film near the protective Pt layer (strap) is unreliable due to significant Ga implantation into the Pt strap during ion beam milling.

XPS depth profiling (roughly a few hundred nm into the film) reveals the elemental composition at the etched position of thin film surface toward to substrate, as shown in figure 14. At the top surface of the thin film (time = 0), the relative atomic composition values of Na, Ti and O are 9%, 26% and 65% respectively, corresponding to a Na:Ti ratio of ca. 0.3 which is close to the Na:Ti ratio in $\text{Na}_2\text{Ti}_6\text{O}_{13}$. The average Na:Ti ratio from XPS within the thin film is about 0.2 which is less than the value at the top surface and is also lower than the average Na:Ti ratio from STEM/EDX data within the film (figure 13). Interestingly, our previous STEM/EDX results on soda lime glass substrates²⁹ suggested an Na/Ti ratio in the film of ca. 0.2. Furthermore, Watanabe et al⁵⁹ report both ordered and disordered sodium titanium dioxide bronzes prepared under hydrothermal conditions based upon a $\text{Na}_{0.8}\text{Ti}_4\text{O}_8$ host framework (i.e. a Na/Ti atomic ratio of 0.2).

Effect of Na content in Substrate Pre-treatment

The %_v of Na in the sodium ethoxide/ethanol solution used in the substrate pre-treatment was varied in order to monitor its effect on titania phase formation in the thin film. XRD patterns from thin films deposited following a range of sodium pre-treatments are shown in figure 15 and reveal that for low sodium concentrations (samples: 0.05%_Si and 0.10%_Si) solely anatase is present. Whilst for concentrations of $\geq 0.16\%$ of Na, the pre-treatment process promoted the formation of $\text{TiO}_2(\text{B})$ as well as the anatase phase, with an increase in the relative proportion of $\text{TiO}_2(\text{B})$ phase with increasing sodium content up to an optimum level of 0.75% Na. This is more clearly seen in figure 16 which shows XRD patterns with the sample tilted off-axis by 2 degrees with respect to a normal 2θ scan. This is to reduce the strength of the single (hkl) reflection from Si wafer substrate which would otherwise dominate the pattern, making it difficult to observe the TiO_2 diffraction peaks.

Approximate phase fractions, using the intensity ratio of the peaks at 24.98° and 25.28° due to the (110) lattice planes of $\text{TiO}_2(\text{B})$ (JCPDS04-007-6246) $\text{TiO}_2(\text{B})$ and the (101) lattice planes of anatase phase (JCPDS00-021-1272) respectively, are given in Table 2. Further increases in Na pre-treatment loadings above the optimum level (0.75% Na) result in the anatase phase becoming the main component in the thin films, although at high loadings (5.0%_Si) the behaviour becomes more complex with the appearance of a crystalline sodium titanate phase ($\text{Na}_2\text{Ti}_6\text{O}_{13}$) apparently at the expense of anatase, as opposed to $\text{TiO}_2(\text{B})$.

Photocatalytic degradation of methylene blue

The photocatalytic activities for methylene blue degradation under UV light irradiation of samples 0%_Si, 0.5%_Si, 1%_Si, 2%_Si and 5%_Si are shown in figure 17 and Table 2. All activities are normalised relative to a catalyst free test (i.e. with no titania). All samples were found to be photocatalytically active, with the highest activity (above that of pure anatase) exhibited by the 2%_Si sample which contained a ratio of TiO₂(B):anatase of 1:2.33, suggesting that a certain proportion of TiO₂(B) in a mixed phase thin film is beneficial for photocatalysis. However, the 0.5%_Na sample, containing the highest proportion of the TiO₂(B) phase (62.2%), showed a decrease in catalytic activity to below that of pure anatase (0%_Si).

The experimental band gaps of anatase and TiO₂(B) phases were determined by Dongjiang et al, 2009 to be 3.19 eV and 3.05 eV respectively.¹³ This implies that there is a difference between the valence band (VB) and/or conduction band (CB) edge potentials of the two phases when they are in intimate contact. Most studies describe that the VB edge potential of anatase is generally lower than that of TiO₂(B) which means, electrons in the VB of anatase can absorb a photon energy more easily than those in TiO₂(B). Therefore, the anatase phase is generally considered to have a higher photocatalytic activity than TiO₂(B). However, mixing anatase/TiO₂(B) has been found to result in a higher photocatalytic efficiency than solely pure anatase. The presence of the two phases, when intimately mixed, possibly enables a charge transfer process between the different phases potentially reducing recombination of photo-generated electrons and so enhancing the photocatalytic activity (figure 18).^{13,14}

Theoretical calculations

The PBE and LDA+OBS calculations are plotted in figure 19, and both data sets reveal that anatase is destabilised by introducing Na interstitials, but that TiO₂(B) is stabilised by the addition of Na. This is a very plausible and intuitive result, consistent with the large voids in B phase and small voids in anatase. The lowest energy site(s) found for Na interstitials in B phase are the same as the most stable site for Li, denoted "site C" (and depicted in Figure 2 of this work) in three of the B phase Li intercalation studies.^{36,37,41} Unlike Arrouvel et al.³⁶ who found small differences of ≤ 0.15 eV between different high-symmetry sites in the B phase unit cell for Li interstitials relative to the most stable "C" site, we found the alternative high-symmetry sites to be vastly unfavourable by well over 1 eV for Na. This is not implausible considering that the van der Waals radius of Na is about 25% larger than that of Li. The data shows that anatase undergoes significant lattice expansion and destabilisation upon being enriched with Na, so extensive diffusion of Na into anatase can be ruled out reasonably confidently. The fact that Na stabilises the B phase, on the other hand, is especially clear from the data, because although a non-zero Na concentration results in positive lattice expansion, the formation energy density still always decreases (that is, becomes more negative) despite the overall volume increase. The PBE results show monotonically increasing B phase volume expansion up to 1.7% at full Na saturation of 7.7 atom%, whereas LDA+OBS exhibits a clear volume expansion maximum of about 0.6% at a threshold Na concentration of about 5 atom%, beyond which the lattice is predicted to contract back towards its pure (0 atom% Na) volume at full Na saturation. We believe that this is due to enhanced attractive Na-Na interactions in the LDA+OBS calculations compared to PBE. The smaller magnitude of the formation energies, smaller changes in the formation energy with Na concentration, and greater volumetric expansion of the PBE results compared to those of the LDA+OBS, are all consistent with the expected slight underbinding tendencies of PBE when compared to the overbinding tendencies of the LDA. In the absence of Na, it is also clear from the data that Ti interstitials destabilise B phase. As a further check, we also studied the case of substituting a bulk-position Ti for a Na using a $1 \times 3 \times 2$ Ti₄₇NaO₉₆ B phase supercell with the PBE functional, and it was found that the total formation energy increased (that is, became less stable) by 13.2 eV, which corresponds to a formation energy density increase of $0.011 \text{ eV \AA}^{-3}$. Thus, the available theoretical evidence firmly rules out any possible role played by Na substitutions and Ti interstitials, and corroborates the original premise: that Na interstitials stabilise bulk B phase and encourage its synthesis. In summary, this theoretical data is evidence that Na is of no consequence for the formation of anatase, but that it plays a critical role in the synthesis of TiO₂(B). These findings are consistent with the experimental observations that i) the presence of Na is a necessary condition for the formation of TiO₂(B) beyond the interface with the substrate, and ii) that Na is quite uniformly distributed throughout films in which TiO₂(B) is present.

The migration barriers ΔE for Na in TiO₂(B) were found to be 2.95 eV in the [100] direction, 2.13 eV along [010] and 2.30 eV along [001], all to 2 d. p. Thus, the lowest energy pathway for Na is along [010], similar to the case found by Arrouvel et al.³⁶ of Li which also showed that the [010] pathway is most favourable, although with a significantly smaller energy barrier of about 0.3 eV. The timescales for migration of Na interstitials between voids can be estimated if the transition rate is assumed to take the form $\Gamma = \nu \exp(-\Delta E/k_B T)$ where $\nu \sim 10^{13}$ Hz is the approximate vibrational frequency of Na and $k_B T = 0.075$ eV (3 d. p.) at $T = 600$ °C. There is an important caveat, however, which is the high sensitivity of the migration rate Γ to changes in the energy barrier ΔE when $\Delta E \gg k_B T$. A hypothetical 1% reduction in the [001] energy barrier from 2.30 eV to 2.277 eV, for example, increases the migration rate by 36%. Due to the convergence from above of the energy barriers, it is likely that the migration rates are at least slightly underestimated. Nevertheless, the migration rates found using the calculated energy barriers ΔE are $\sim 10^{-4} \text{ s}^{-1}$ along [100], $\sim 10^1 \text{ s}^{-1}$ along [010] and $\sim 10^0 \text{ s}^{-1}$ along [001].

Indeed, the theoretical insight gained here does not explain the observed increase in the relative proportion of anatase formation beyond 0.75% Na concentration in the pre-treatment solution, so while it is certainly likely that Na stabilises TiO₂(B), more intimate knowledge of the atomic-scale structural arrangements of the intermediate sodium titanate layer depicted in figure 19 is necessary for a full theoretical

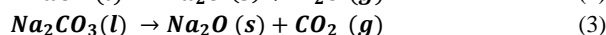
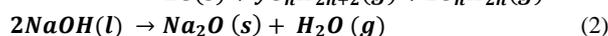
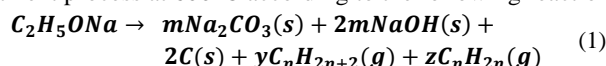
understanding. In principle, detailed structural information on Na site positions in the structure could be experimentally achieved via direct imaging using high angle annular dark field (HAADF) STEM combined with Electron Energy Loss Spectroscopy (EELS) and image simulation and spectral modelling. However, this is currently challenging due to mobility of Na under high flux electron probes.

Discussion

Previously we investigated TiO₂(B) phase formation in thin films deposited by LPCVD onto soda-lime glass substrates,²⁹ where our findings suggested a mechanism involving diffusion of Na⁺ ions out of the substrate to form an intermediate layer at the interface which subsequently decomposed into the TiO₂(B) phase. Here we have extended this work to investigate whether substrates that are sodium-free could be pre-treated with sodium so as to promote TiO₂(B) formation during LPCVD. The present results demonstrate that mixed phase TiO₂(B)/anatase thin films can be prepared on any general substrate using a modified LPCVD method involving pre-treatment of the substrate by a sodium spraying method using NaOEt in Ethanol.

We propose a potential three-step mechanism for TiO₂(B) formation as illustrated schematically in figure 20:

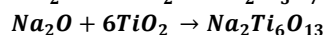
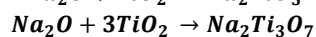
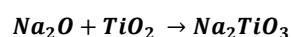
(1) The substrate was first prepared by spraying sodium ethoxide solution onto the substrate surface. Sodium ethoxide thermally decomposes during the pre-heat treatment process at 600°C according to the following reaction:⁶⁰⁻⁶²



As in equation 1, the initial decomposition step of sodium ethoxide at 1 atm in air typically occurs above 300°C and produces hydrocarbon gases, amorphous carbon and two main residues: sodium carbonate and sodium hydroxide in the mole ratio 1:2.60 Above 320°C, NaOH melts and decomposes to form a thin layer of Na₂O and steam (equation 2).⁶² Above a temperature of 850°C Na₂CO₃ can also generate Na₂O,^{63,64} as shown in equation 3; however at low pressure this decomposition temperature may be reduced. Furthermore, decomposition reactions of metal carbonates are partially reversible reactions and the removal of gas phase of products by the vacuum system may encourage an increase in the forward reaction rate;

(2) During the LPCVD process itself, we suggest that this Na₂O layer will react with the nascent TiO₂ film formed by the decomposition of TTIP its subsequent deposition, forming an intermediate phase. Unfortunately the nature of this intermediate phase is not known, as it is not practical or possible to quench the LPCVD reaction and “freeze in” reaction intermediates to allow their structural or chemical determination. The intermediate phase will necessarily contain sodium, titanium and oxygen and would appear to promote the ultimate crystallisation of a (Na-doped) TiO₂(B) phase, as predicted by our DFT results which have shown that Na stabilizes the monoclinic TiO₂(B) structure. At high Na loadings (5.0%_{Si} sample), this intermediate phase also promotes crystallisation of Na₂Ti₆O₁₃ (figure 16).

Possibilities for this intermediate phase include: an ordered or disordered sodium titanate bronze (similar to that described by Watanabe et al.⁵⁹ which was based on Na_{0.8}Ti₄O₈ host framework) or a crystalline monoclinic sodium titanate with a tunnel structure such as Na₂TiO₃, Na₂Ti₃O₇ and Na₂Ti₆O₁₃. According to a binary phase diagram for the Na₂O-TiO₂ system,⁶⁵ each of these intermediate sodium titanates could be formed at 600°C depending on the exact Na₂O/TiO₂ phase ratio present, as shown in the following reactions:



In the hydrothermal synthesis work of Watanabe et al., at low temperatures (<300°C) a disordered sodium titanate bronze of variable sodium content was observed. Above 350°C this sodium titanate bronze became ordered in terms of the sodium distribution and possible inclusion of water. Above 450°C, the ordered bronze phase (having released water) was found to co-exist with Na₂Ti₉O₁₉, Na₂Ti₆O₁₃ and Na₂Ti₃O₇ (with increasing Na content respectively).

Based on the current levels of Na employed in the current study and the temperature, we believe that a dehydrated, ordered sodium titanate bronze (of variable sodium content) together with possibly Na₂Ti₆O₁₃ are the most likely crystalline intermediate phases to be formed. We denote this in figure 20 as simply Na_xTi_yO_z. This phase could act as a seeding material for TiO₂(B) formation.^{6,66,67} In these structures, typically Na⁺ ions are located in the interlayers between negatively charged sheets composed of TiO₆ octahedral building blocks as shown in figure 21 for Na₂Ti₆O₁₃. If these Na⁺ ions are mobile, then their migration out of the structure may effectively template a TiO₂ tunnel structure which may subsequently rearrange to form TiO₂(B). We note that theoretically there is an approximate orientation relationship between the monoclinic Na₂Ti₆O₁₃ phase and the monoclinic TiO₂(B) phase: B phase (001) plane parallel with the sodium titanate (-101) plane, and B phase [-100] direction parallel to the sodium titanate [301] direction. We also note that the sodium titanate and TiO₂(B) structures can be interconverted by crystallographic shear of the (002) titanate plane along ¼ [100] (see figure 21).

(3) Sodium ions in the seeding structure continuously migrate into the newly deposited layers of TiO₂ and promote TiO₂(B) formation; in some ways this is analogous to a root and/or tip growth mechanism characteristic of carbon nanotube synthesis using (metal) catalytic chemical vapor deposition.⁶⁸ However, in the absence of a significant quantity of Na, the deposited titania will form

the anatase phase instead of TiO₂(B). This general hypothesis is supported by our previous findings regarding TiO₂(B) formation promoted by Na⁺ diffusion from soda-lime glass substrates under the same synthesis conditions.²⁹ However, using the pre-treatment process it would appear that sodium diffuses rapidly through the film and TiO₂(B) is not just confined to the interfacial region adjacent to the substrate, nor does it grow in an oriented fashion as is the case for soda lime glass substrates.

As mentioned in the introduction, a number of studies have reported the improved photocatalytic efficiency of mixed phase TiO₂(B)/anatase over either commercial P25 (mixed phase anatase and rutile) or single phase TiO₂ (anatase, rutile, brookite and TiO₂(B)). This has been investigated for several photocatalyst reactions including: methyl orange-,^{69,70} sulforhodamine B-,^{13,14} methylene blue-^{5,71,72} and yellow XRG dry-⁷³ degradations; nitrate reduction;⁷⁴ acetaldehyde decomposition⁷⁵ and the water splitting reaction.⁷⁶ Our current results, albeit preliminary, indicate an enhanced catalytic activity for mixed phase thin films which contained an approximately 1:2 ratio of TiO₂(B):anatase. Potential ways to improve this photocatalytic activity potentially include: a more intimate mixing of the two phases of TiO₂, as well as increasing the overall surface area via an introduction of porosity or nanostructuring into the thin film. Further more complex photocatalytic tests based on water splitting are planned in the future. For the practical application of TiO₂ photo-catalysts, the ability to produce thin films of mixed phase TiO₂(B) and anatase on rigid substrates may be beneficial owing to their ability to be reused whilst retaining high catalyst performance.

In the case of anode materials, mixed phase TiO₂(B) and anatase thin films on anodes may offer improved Li ion battery performance. Lithium can diffuse into both the anatase and TiO₂(B) frameworks in three dimensions through open channels or voids within the structures;^{77,78} however TiO₂(B) provides the highest percentage of voids amongst the TiO₂ polymorphs and nano-TiO₂(B) is able to accommodate 1 Li⁺ per Ti which is higher than that for anatase.⁷⁹ However, for the TiO₂(B) phase a significant irreversible capacity loss occurs at the initial charge-discharge cycle, whereas in anatase this effect is smaller.^{78,80} Thus, the ability to produce a thin, high surface area film with some mesoporosity and containing a combination of both polymorphs may ultimately improve overall anode performance.

Conclusions

Titania thin films consisting of a mixed phase TiO₂(B)/anatase were successfully synthesized by a modified LPCVD route involving pre-treatment of the substrates by a sodium spraying method using NaOEt in Ethanol. A number of different substrates including fused quartz, Si wafer, HOPG and grafoil were deposited with around 400 nm thick mixed phase titania films using 5 mL of a TTIP precursor for 15 min at nominal temperature of 600 °C. The optimum Na concentration of the sodium ethoxide/ethanol solution in the pre-treatment process so as to promote the highest amount of TiO₂(B) phase composition in the thin films, was found to be 0.75% w/v. Theoretical calculations suggest that the presence of Na in interstitial positions within voids in the structure stabilises the TiO₂(B) structure rather than anatase. A mechanism for modified LPCVD preparation of TiO₂(B) is proposed involving the decomposition of the thin Na-containing layer and migration of Na⁺ ions into the TiO₂ layer to form an intermediate sodium titanate phase. A mixed phase thin film of specific composition was shown to have enhanced photocatalytic activity for simple dye degradation. Potentially this thin film fabrication process could be utilised with any desired substrate to produce tailored mixed phase titania compositions for application as either photocatalytic thin films or anode materials for lithium ion batteries.

Acknowledgements

We would like to thank the Ministry of Science and Technology, the Royal Thai Government for a scholarship to Yothin Chimupala and the Thailand Research Fund (TRF) for providing financial support through the Royal Golden Jubilee Ph.D program to Patcharanan Junploy. We also thank Dr Geoff Hyett at Southampton University and Mr. Robert Simpson at Leeds University for help in initiating this research. Trevor Hardcastle would like to thank the EPSRC for the Doctoral Prize Fellowship which funded this research in part. Theoretical calculations were undertaken using the high performance computing facilities ARC1 and ARC2 at The University of Leeds.

Extended Footnote †

In all calculations ultrasoft pseudopotentials⁸¹ were used with a plane wave cutoff energy of 400 eV and Monkhorst-Pack k-point grids⁸² with spacings not exceeding 0.04 Å⁻¹ to converge all interatomic forces to within 0.03 eVÅ⁻¹ using BFGS minimisation.⁸³⁻⁸⁷ All supercells were built using separately optimised B phase and anatase bulk unit cells whose lattice parameters were optimised to a = 12.2796 Å, b = 3.7551 Å, c = 6.6258 Å (4 d. p.) for TiO₂(B), and a = b = 3.7991 Å and c = 9.7155 Å (4 d. p.) for anatase using PBE, and a = 12.0234 Å, b = 3.6873 Å, c = 6.4523 Å (4 d. p.) for TiO₂(B), and a = b = 3.7346 Å and c = 9.3710 Å (4 d. p.) for anatase using LDA+OBS. Comparing these with published X-ray diffraction values for TiO₂(B):⁸⁸ a_{exp} = 12.163(5) Å, b_{exp} = 3.735(2) Å, c_{exp} = 6.513(2) Å (4 d. p.), and for anatase:⁸⁹ a_{exp} = 3.7892 Å, c_{exp} = 9.5370 Å (4 d. p.), confirms the over- and underestimation of

the optimised lattice parameters consistent with the expected under- and overbinding characteristics of the PBE and LDA(+OBS) functionals respectively.

Notes and References

- 1 A. Fujishima, T. N. Rao and D. A. Tryk, *J. Photochem. Photobiol. C Photochem. Rev.*, 2000, **1**, 1.
- 2 T. Watanabe, H. Hayashi and H. Imai, *Sol. Energy Mater. Sol. Cells*, 2006, **90**, 640.
- 3 G. Pfaff and P. Reynnders, *Chem. Rev.*, 1999, **99**, 1963.
- 4 X. Zhao, Q. Zhao, J. Yu and B. Liu, *J. Non. Cryst. Solids*, 2008, **354**, 1424.
- 5 V. Etacheri, J. E. Yourey and B. M. Bartlett, *ACS Nano*, 2014, **8**, 1491.
- 6 Z. Guo, X. Dong, D. Zhou, Y. Du, Y. Wang and Y. Xia, *RSC Adv.*, 2013, **3**, 3352.
- 7 F. Wu, X. Li, Z. Wang and H. Guo, *Nanoscale*, 2013, **5**, 6936.
- 8 S. W. Oh, S.-H. Park and Y.-K. Sun, *J. Power Sources*, 2006, **161**, 1314.
- 9 P. Roy and S. K. Srivastava, *J. Mater. Chem. A*, 2015, **3**, 2454.
- 10 M. Søndergaard, Y. Shen, A. Mamakhel, M. Marinaro, M. Wohlfahrt-Mehrens, K. Wonsyld, S. Dahl and B. B. Iversen, *Chem. Mater.*, 2015, **27**, 119.
- 11 L. K. Barbora Laskova, Marketa Zukalava, Arnost Zukal, Milan Bousa, *J. Power Sources*, 2014, **246**, 103.
- 12 Z. Liu, Y. G. Andreev, A. R. Armstrong, S. Brutti, Y. Ren and P. G. Bruce, *Prog. Nat. Sci. Mater. Int.*, 2013, **23**, 235.
- 13 D. Yang, H. Liu, Z. Zheng, Y. Yuan, J. Zhao, E. R. Waclawik, X. Ke and H. Zhu, *J. Am. Chem. Soc.*, 2009, **131**, 17885.
- 14 Z. Zheng, H. Liu, J. Ye, J. Zhao, E. R. Waclawik and H. Zhu, *J. Mol. Catal. A Chem.*, 2010, **316**, 75.
- 15 M. Fehse, F. Fischer, C. Tessier, L. Stievano and L. Monconduit, *J. Power Sources*, 2013, **231**, 23.
- 16 V. Etacheri, R. Marom, R. Elazari, G. Salitra and R. Aurbach, *Energy Environ. Sci.*, 2011, **4**, 3243.
- 17 Y. Qi and S. J. Harris, *J. Electrochem. Soc.*, 2010, **157**, A741.
- 18 Y. Reynier, R. Yazami, B. Fultz and I. Barsukov, *J. Power Sources*, 2007, **165**, 552.
- 19 Y. Qi, H. Guo, L. G. Hector and A. Timmons, *J. Electrochem. Soc.*, 2010, **157**, A558.
- 20 Y. Ren, Z. Liu, F. Pourpoint, A. R. Armstrong, C. P. Grey and P. G. Bruce, *Angew. Chemie Int. Ed.*, 2012, **51**, 2164.
- 21 G. Armstrong, A. R. Armstrong, J. Canales and P. G. Bruce, *Chem. Commun.*, 2005, 2454.
- 22 S. Liu, H. Jia, L. Han, J. Wang, P. Gao, D. Xu, J. Yang and S. Che, *Adv. Mater.*, 2012, **24**, 3201.
- 23 C. J. Tavares, J. Vieira, L. Rebouta, G. Hungerford, P. Coutinho, V. Teixeira, J. O. Carneiro and a. J. Fernandes, *Mater. Sci. Eng. B*, 2007, **138**, 139.
- 24 P. Löbl, M. Huppertz and D. Mergel, *Thin Solid Films*, 1994, **251**, 72.
- 25 R. Álvarez, L. González-García, P. Romero-Gómez, V. Rico, J. Cotrino, A. R. González-Elipse and A. Palmero, *J. Phys. D. Appl. Phys.*, 2011, **44**, 385302.
- 26 H. Lin, A. K. Rumaiz, M. Schulz, D. Wang, R. Rock, C. P. Huang and S. I. Shah, *Mater. Sci. Eng. B*, 2008, **151**, 133.
- 27 A. J. Cross, C. W. Dunnill and I. P. Parkin, *Chem. Vap. Depos.*, 2012, **18**, 133.
- 28 G. Hyett, M. Green and I. P. Parkin, *J. Am. Chem. Soc.*, 2006, **128**, 12147.
- 29 Y. Chimupala, G. Hyett, R. Simpson, R. Mitchell, R. Douthwaite, S. J. Milne and R. D. Brydson, *RSC Adv.*, 2014, **4**, 48507.
- 30 M. Ben Yahia, F. Lemoigno, T. Beuvier, J.-S. Filhol, M. Richard-Plouet, L. Brohan and M.-L. Doublet, *J. Chem. Phys.*, 2009, **130**, 204501.
- 31 V. Swamy, J. D. Gale and L. S. J. Dubrovinsky, *Phys. Chem. Solids* 2001, **62**, 887
- 32 A. Vittadini, M. Casarin and A. Selloni *J. Phys. Chem. C* 2009, **113**, 18973
- 33 A. Vittadini, M. Casarin and A. Selloni, *J. Mater. Chem.* 2010, **20**, 5871
- 34 G. Nuspl, K. Yoshizawa and T. Yamabe, *J. Mater. Chem.* 1997, **7**, 2529
- 35 D. Panduwinata and J. D. Gale, *J. Mater. Chem.* 2009, **19**, 3931
- 36 C. Arrouvel, S. C. Parker and M. S. Islam, *Chem. Mater.* 2009, **21**, 4778
- 37 A. R. Armstrong, C. Arrouvel, V. Gentili, S. C. Parker, M. S. Islam and P. G. Bruce, *Chem. Mater.*, 2010, **22**, 6426
- 38 M. V. Koudriachova, *Surf. Interface Anal.*, 2010, **42**, 1330
- 39 A. G. Dylla, P. H. Xiao, G. Henkelman and K. J. Stevenson, *J. Phys. Chem. Lett.*, 2012, **3**, 2015
- 40 A. S. Dalton, A. A. Belak and A. Van der Ven, *Chem. Mater.*, 2012, **24**, 1568
- 41 B. J. Morgan and P. A. Madden, *Phys. Rev. B*, 2012, **86**, 035147
- 42 F. De Angelis, C. Di Valentin, S. Fantacci, A. Vittadini and A. Selloni, *Chem. Rev.*, 2014, **114**, 9708
- 43 P. Hohenberg and W. Kohn, *Phys. Rev.*, 1964, **136**, B864
- 44 W. Kohn and L. J. Sham, *Phys. Rev.*, 1965, **140**, A14433
- 45 S. J. Clark, M. D. Segall, C. J. Pickard, P. J. Hasnip, M. J. Probert, K. Refson and M. C. Payne, *Z. Kristallogr.*, 2005, **220**, 567
- 46 X.-Q. Gong, A. Selloni, *Phys. Rev. B*, 2007, **76**, 235307.
- 47 J. Muscat, V. Swamy and N. M. Harrison, *Phys. Rev. B*, 2002, **65**, 224112.
- 48 F. Labat, P. Baranek, C. Domain, C. Minot and C. Adamo, *J. Chem. Phys.*, 2007, **126**, 154703.
- 49 M. R. Ranade, A. Navrotsky, H. Z. Zhang, J. F. Banfield, S. H. Elder, A. Zaban, P. H. Borse, S. K. Kulkarni, G. S. Doran and H. J. Whitfield, *Proc. Nat. Acad. Sciences*, 2002, **99**, 6476
- 50 J. P. Perdew, K. Burke and M. Ernzerhof *Phys. Rev. Lett.*, 1996, **77**, 3865
- 51 F. Ortmann, F. Bechstedt and W. G. Schmidt, *Phys. Rev. B*, 2006 **73**, 205101
- 52 T. A. Halgren and W. N. Lipscomb, *Chem. Phys. Lett.*, 1977, **49**, 225
- 53 N. Govind, M. Peterson, G. Fitzgerald, D. K-Smith, and J. Andzelm, *Comput. Mater. Sci.*, 2003, **28**, 250
- 54 S. Reich and C. Thomsen, *Philos. Trans. A. Math. Phys. Eng. Sci.*, 2004, **362**, 2271.
- 55 T. Ohsaka, F. Izumi and Y. Fujiki, *J. Raman Spectrosc.*, 1978, **7**, 321.

- 56 T. Beuvier, M. Richard-plouet and L. Brohan, *J. Phys. Chem. C*, 2009, **113**, 13703.
- 57 T. Beuvier, M. Richard-Plouet and L. Brohan, *J. Phys. Chem. C*, 2010, **114**, 7660.
- 58 V. K. Singh, *J. Vac. Sci. Technol. A Vacuum, Surfaces, Film.*, 1993, **11**, 557.
- 59 M. Watanabe and E. Watanabe, *J. Solid State Chem.*, 1980, **32**, 233.
- 60 K. Chandran, M. Kamruddin, P. K. Ajikumar, A. Gopalan and V. Ganesan, *J. Nucl. Mater.*, 2006, **358**, 111.
- 61 K. Chandran, M. Kamruddin, P. K. Ajikumar, A. Gopalan and V. Ganesan, *J. Nucl. Mater.*, 2008, **374**, 158.
- 62 V. P. Yurinskii, E. G. Firsova and S. A. Proskura, *Russ. J. Appl. Chem.*, 2005, **78**, 360.
- 63 A. E. Newkirk and I. Aliferis, *Anal. Chem.*, 1958, **30**, 982.
- 64 A. M. Thomas, *J. Chem. Eng. Data*, 1963, **8**, 51.
- 65 R. Bouaziz, M. Mayer and C. R. Hebd, *Seances Acad. Sci. Ser. C.*, 1971, **23**, 1874.
- 66 T. P. Feist and Peter K. Davies, *J. Solid State Chem.*, 1992, **101**, 275.
- 67 V. Etacheri, Y. Kuo, A. Van der Ven and B. M. Bartlett, *J. Mater. Chem. A*, 2013, **1**, 12028.
- 68 M. Kumar and Y. Ando, *J. Nanosci. Nanotechnol.*, 2010, **10**, 3758.
- 69 C. Huang, K. Zhu, M. Qi, Y. Zhuang and C. Cheng, *J. Phys. Chem. Solids*, 2012, **73**, 757.
- 70 G. Xiang, T. Li, J. Zhuang and X. Wang, *Chem. Commun.*, 2010, **46**, 6801.
- 71 C.-W. Peng, M. Richard-Plouet, T.-Y. Ke, C.-Y. Lee, H.-T. Chiu, C. Marhic, E. Puzenat, F. Lemoigno and L. Brohan, *Chem. Mater.*, 2008, **20**, 7228.
- 72 H. Song, H. Jiang, T. Liu, X. Liu and G. Meng, *Mater. Res. Bull.*, 2007, **42**, 334.
- 73 J. Zhu, J. Zhang, F. Chen and M. Anpo, *Mater. Lett.*, 2005, **59**, 3378.
- 74 M. M. Mohamed, B. H. M. Asghar and H. A. Muathen, *Catal. Commun.*, 2012, **28**, 58.
- 75 C. Wang, X. Zhang and Y. Liu, *Nanoscale*, 2014, **6**, 5329.
- 76 K. Kiatkittipong, A. Iwase, J. Scott and R. Amal, *Chem. Eng. Sci.*, 2013, **93**, 341.
- 77 C. Jiang and J. Zhang, *J. Mater. Sci. Technol.*, 2013, **29**, 97–122.
- 78 D. Deng, M. G. Kim, J. Y. Lee and J. Cho, *Energy Environ. Sci.*, 2009, **2**, 818.
- 79 A. G. Dylla, G. Henkelman and K. J. Stevenson, *Acc. Chem. Res.*, 2013, **46**, 1104.
- 80 M. Wagemaker and F. M. Mulder, *Acc. Chem. Res.*, 2013, **46**, 1206.
- 81 D. Vanderbilt, *Phys. Rev. B* 1990, **41**, 7892
- 82 H. J. Monkhorst and J. D. Pack, *Phys. Rev. B* 1976, **13**, 5188
- 83 C. G. Broyden, *IMA J. Appl. Math.* 1970, **6**, 76
- 84 C. G. Broyden, *IMA J. Appl. Math.* 1970, **6**, 222
- 85 R. Fletcher, *Comp. J.*, 1970, **13**, 317
- 86 D. Goldfarb, *Math. Comp.* 1970, **24**, 23
- 87 D. F. Shanno, *Math. Comp.* 1970, **24**, 647
- 88 T. P. Feist and P. K. Davies, *J. Solid State Chem.* 1992, **101**, 275
- 89 M. Horn, C. F. Schwerdtfeger and E. P. Meagher, *Z. Kristallogr. – Cryst. Mat.* 1972, **136**, 273

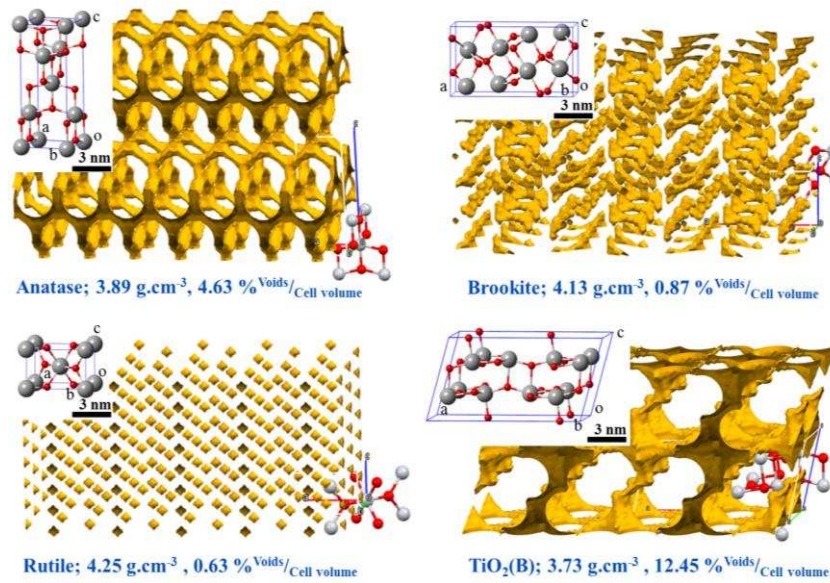


Fig. 1 Crystal voids within the structures of the TiO₂ polymorphs showing the available voids (yellow shading) and their relative percentage volume calculated using Crystal Explorer with an isovalue of 0.008 e.au⁻³ (standard pore size for Li insertion).¹⁰ Anatase and TiO₂(B) exhibit interconnected void structures whereas rutile and brookite possess isolated voids.

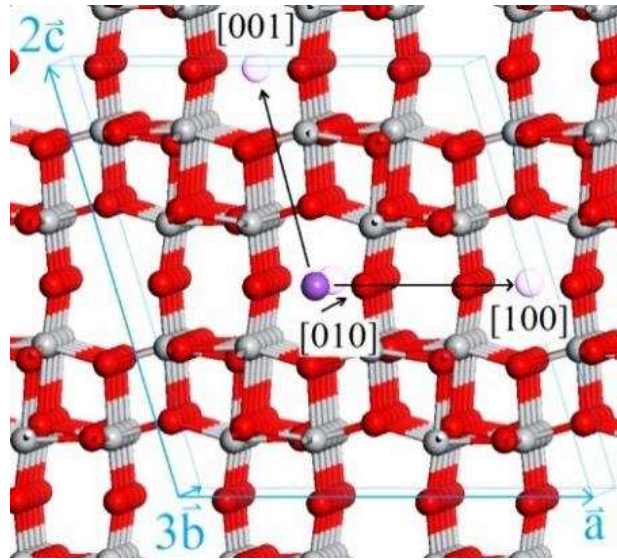


Fig. 2 The three Na interstitial migration pathways $[001]$, $[010]$ and $[100]$ illustrated within a ball and stick model showing a $1 \times 3 \times 2$ supercell of chemical formula $\text{Ti}_{48}\text{O}_{96}\text{Na}$ with lattice vectors indicated in blue. O and Ti ions are illustrated in red and silver respectively.

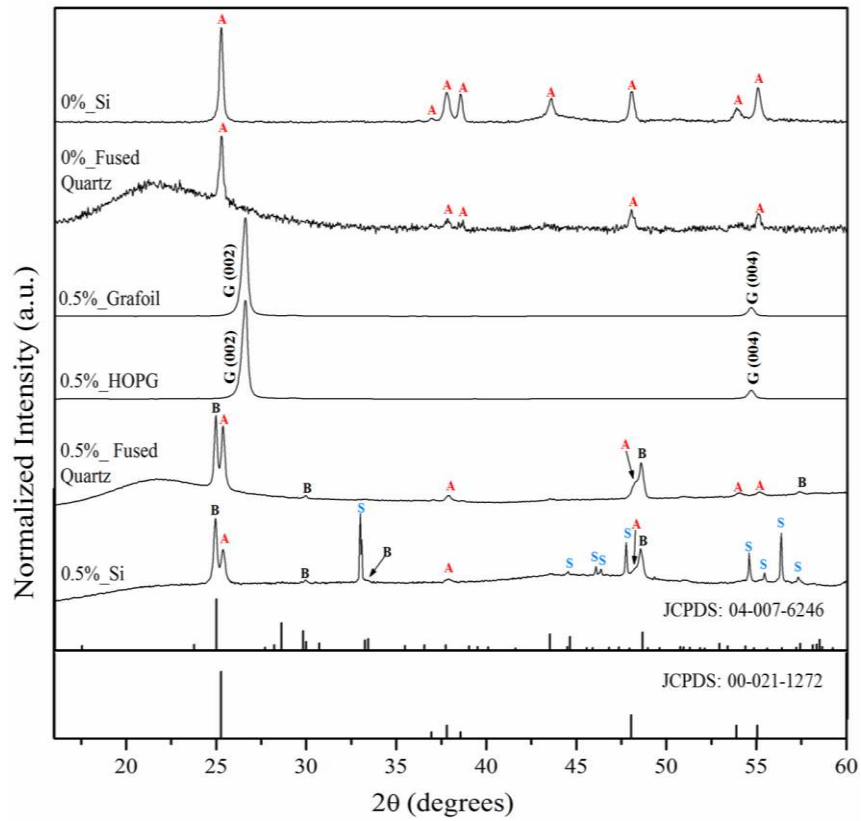


Fig. 3 XRD patterns of TiO₂ thin films deposited onto four different substrates: Si wafer, fused quartz, HOPG and Grafoil; A, B, S and G refer to peak assignments to TiO₂ anatase phase, TiO₂(B) phase, Si substrate and graphite substrate respectively. In addition to control experiments with Na pre-treatment (0%_Si), the substrates were first prepared with a very thin layer of Na-containing compound via spraying a 0.5%^{w/v} sodium solution onto the substrate surfaces.

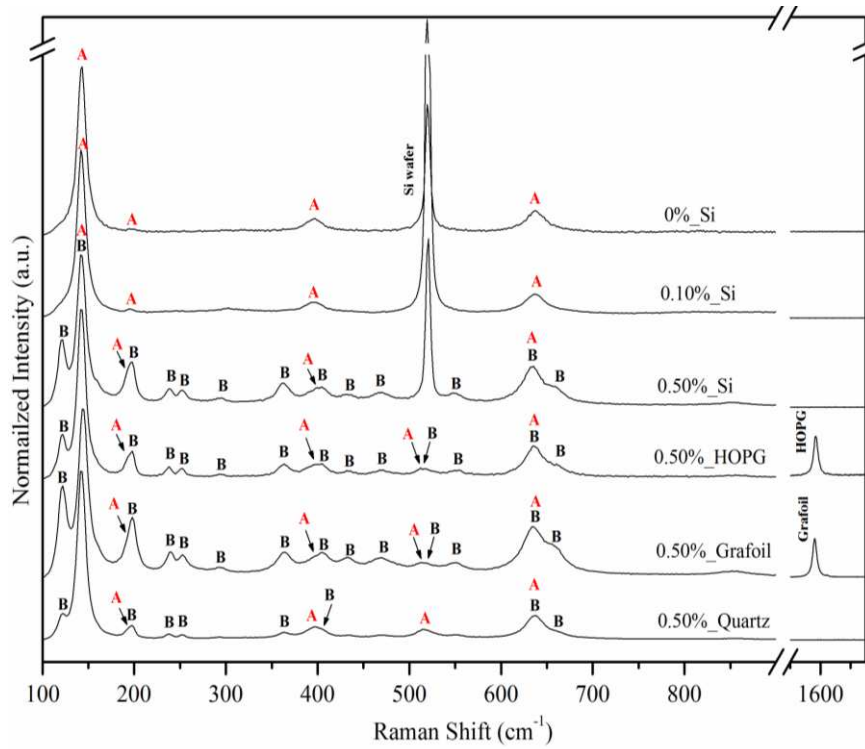


Fig. 4 Raman spectra of TiO₂ thin films deposited onto four different pre-treated substrates: Si wafer, fused quartz, HOPG and Grafoil, in addition a TiO₂ thin film deposited on a bare Si wafer substrate (0%_Si) is included for reference; A and B indicate peaks due to the anatase and TiO₂(B) phases respectively.

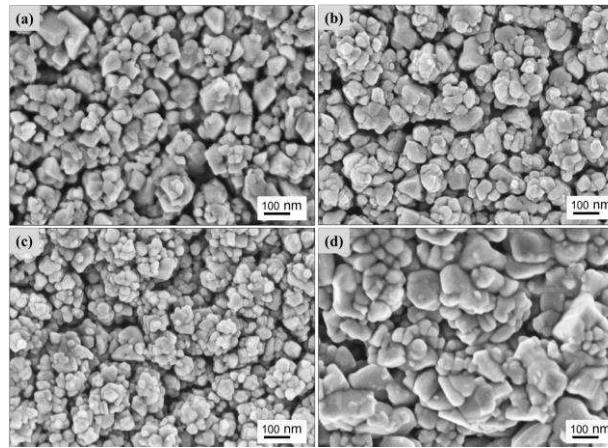


Fig. 5 SEM secondary electron images of TiO₂ particles from the top surface of thin films samples: (a) 0.5%_Si (b) 0.5%_fused quartz (c) 0.5%_HOPG and (d) 0.5%_Grafoil respectively.

Table 1 List of synthesised samples with results of SEM/EDX quantitative elemental analysis, XRD crystallite size and primary particle size and film thickness derived from SEM.

Sample	Composition in Atom%					Calculated XRD crystallite size - Scherrer's equation (nm)		Measured primary particle size (nm)	Approximate % porosity from SEM image analysis	Measured film thickness (μm)
	from SEM/EDX					TiO ₂ (B)	Anatase			
	Na	Si	Ti	O	C					
0.5%_Si	0.68	11.19	22.39	60.41	5.33	42 \pm 5	30 \pm 5	56.3 \pm 1.2 (S.D=19.8)	25.5	0.463 \pm 0.003 (S.D=0.024)
0.5%_Fused quartz	1.67	31.85	9.73	48.98	7.77	40 \pm 5	35 \pm 5	49.7 \pm 1.2 (S.D=18.6)	16.8	0.650 \pm 0.003 (S.D=0.023)
0.5%_HOPG	0.95	0	16	46.86	36.19	N/A	N/A	44.1 \pm 1.2 (S.D=15.8)	17.8	0.485 \pm 0.003 (S.D=0.018)
0.5%_Grafoil	0.29	0	14.31	45.76	39.64	N/A	N/A	91.7 \pm 1.2 (S.D=64.4)	15.7	2.068 \pm 0.003 (S.D=0.209)

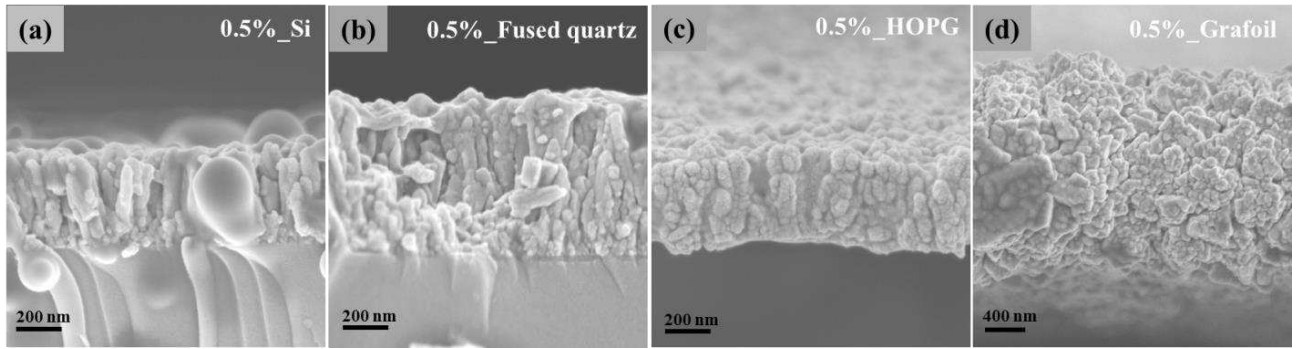


Fig.6 SEM cross-sectional images of TiO₂ thin films deposited on: (a) Si wafer (b) fused quartz (c) HOPG and (d) Grafoil substrates

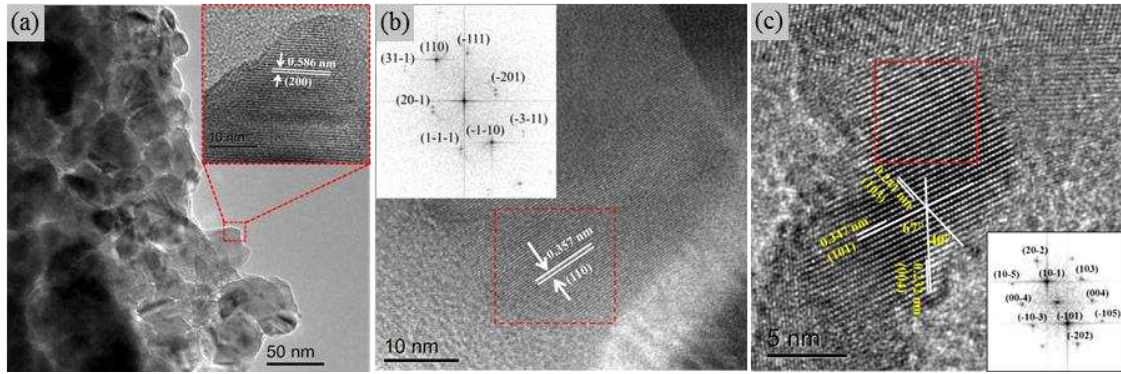


Fig.7 (a) A bright field TEM image taken from 0.5%_Si, showing an equi-axed particle morphology; (b) a HRTEM image of a $\text{TiO}_2(\text{B})$ particle and (c) a HRTEM image of anatase particles, both with the corresponding fast Fourier transforms of the image inset.

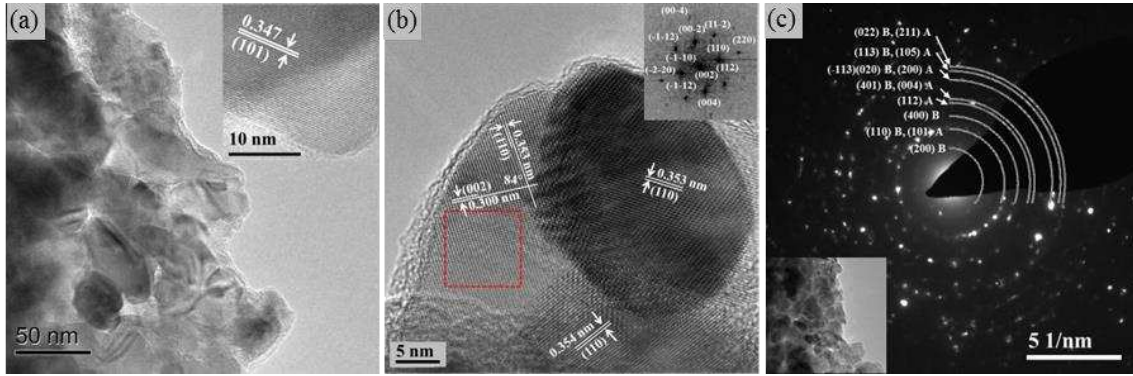


Fig.8 (a) A bright field TEM image taken from 0.5%_Fused quartz; (b) a HRTEM image of $\text{TiO}_2(\text{B})$ with corresponding fast Fourier transform of the image inset; (c) a diffraction pattern of a group of particles shown in the image inset.

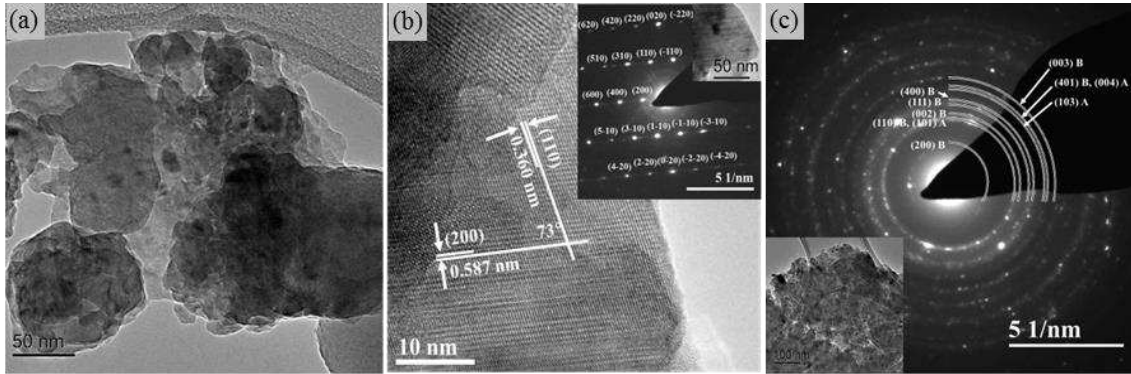
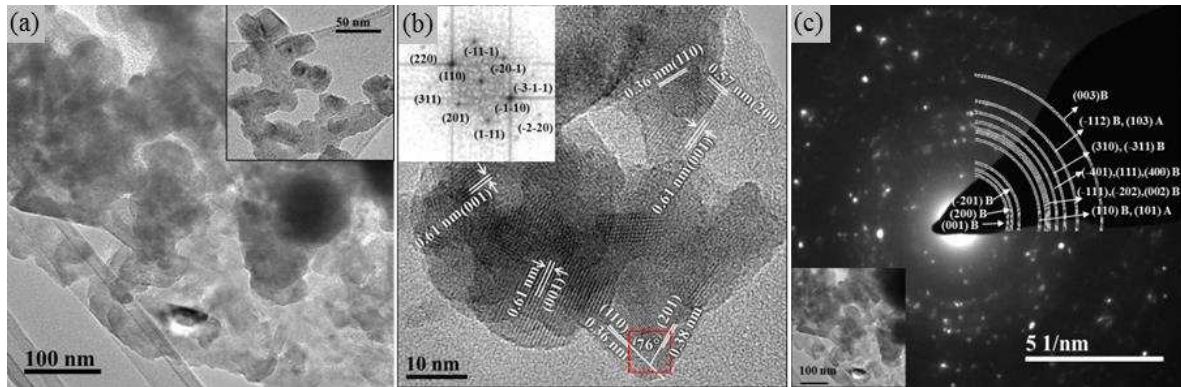
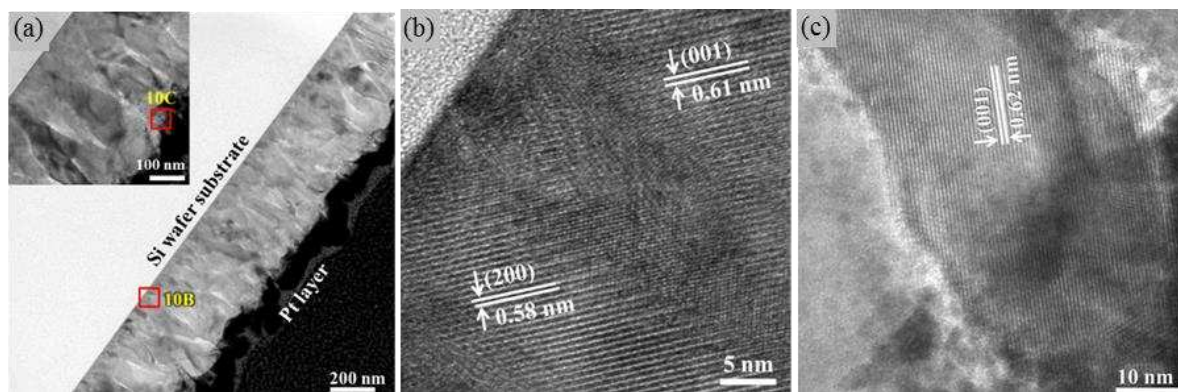


Fig.9 (a) A typical TEM image taken from 0.5%_HOPG; (b) a HRTEM image of a $\text{TiO}_2(\text{B})$ particle with associated electron diffraction pattern; (c) diffraction pattern taken from a group of particles shown in the image inset.



ig.10 (a) A bright field TEM image taken from 0.5%_Grafoil; (b) a HRTEM image of a group of $\text{TiO}_2(\text{B})$ with corresponding fast Fourier transform of the image inset; (c) a diffraction pattern of a group of particles shown in the image inset.



g.11 (a) A TEM image of a FIB cross-section of 0.5%_Si; (b) corresponding HRTEM image at the TiO₂/Si wafer interface labeled as 10B in (a); (c) HRTEM image taken from the TiO₂/protective Pt layer interface labeled as 10C in (a).

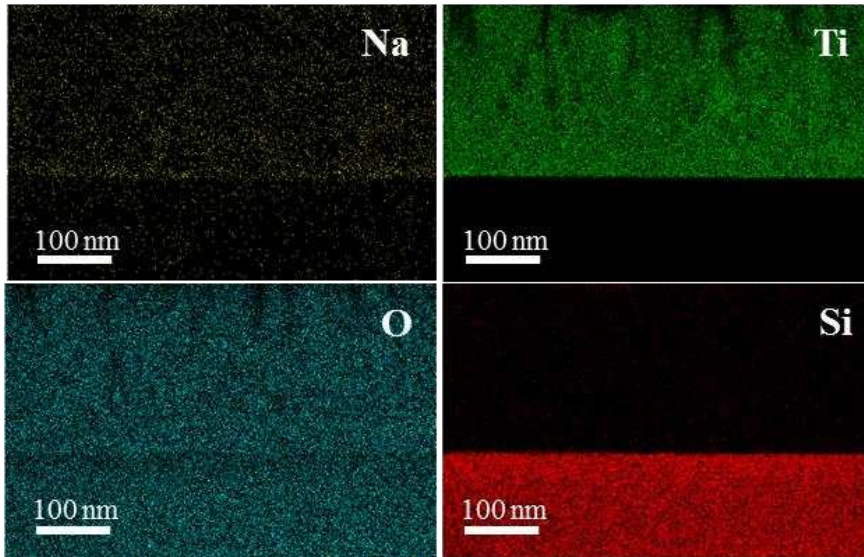
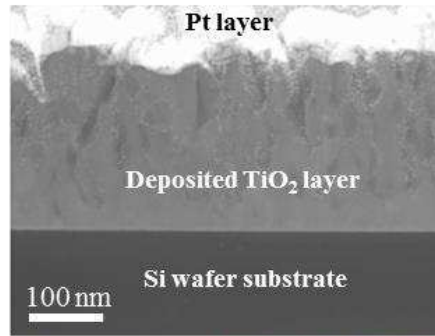


Fig. 12 STEM-EDX elemental maps from the FIB cross-sectional sample of 0.5%_Si, showing the elemental distribution in the thin film and the TiO₂/Si wafer interfacial areas.

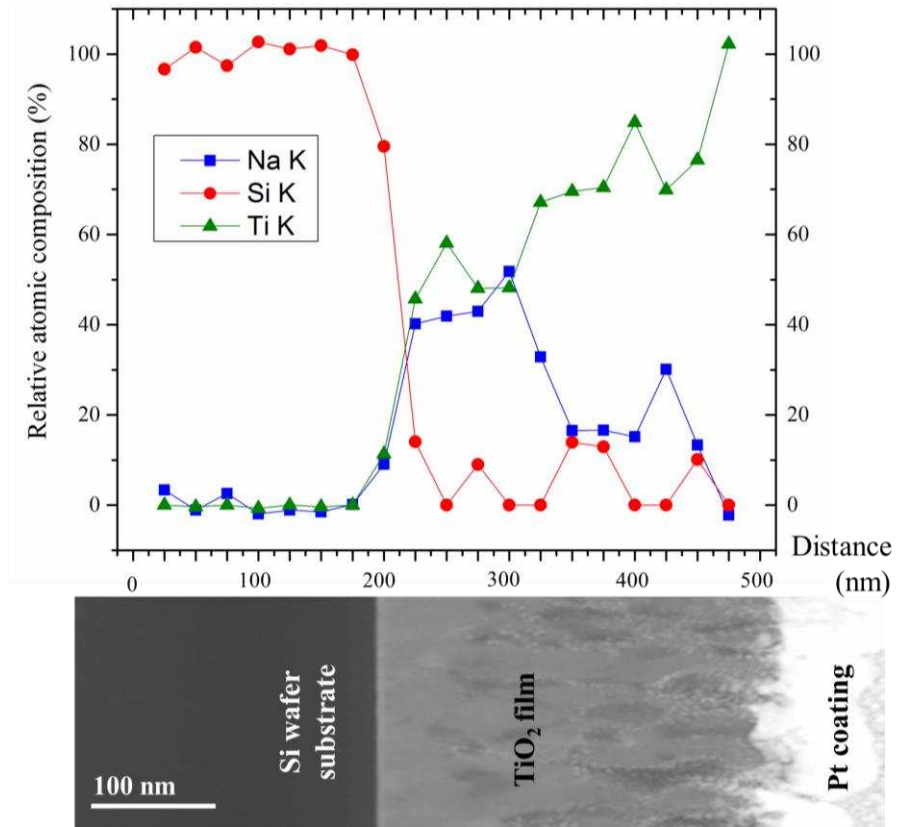


Fig. 13 STEM-EDX line scan of FIB cross section of 0.5%_Si sample.

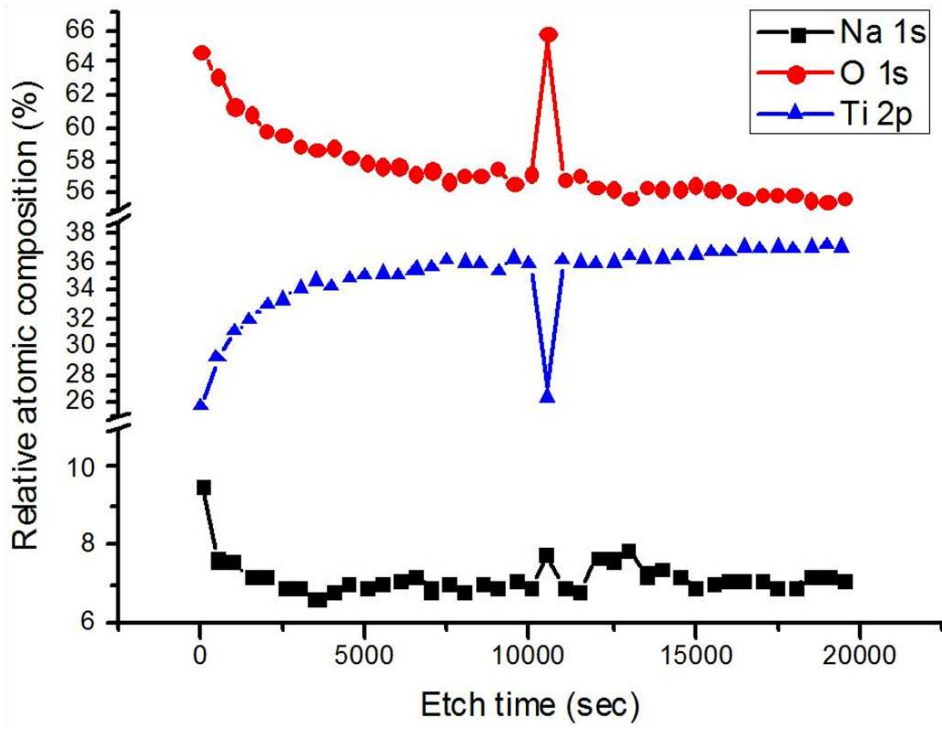


Fig. 14 X-ray Photoelectron spectroscopy depth profile from the film surface.

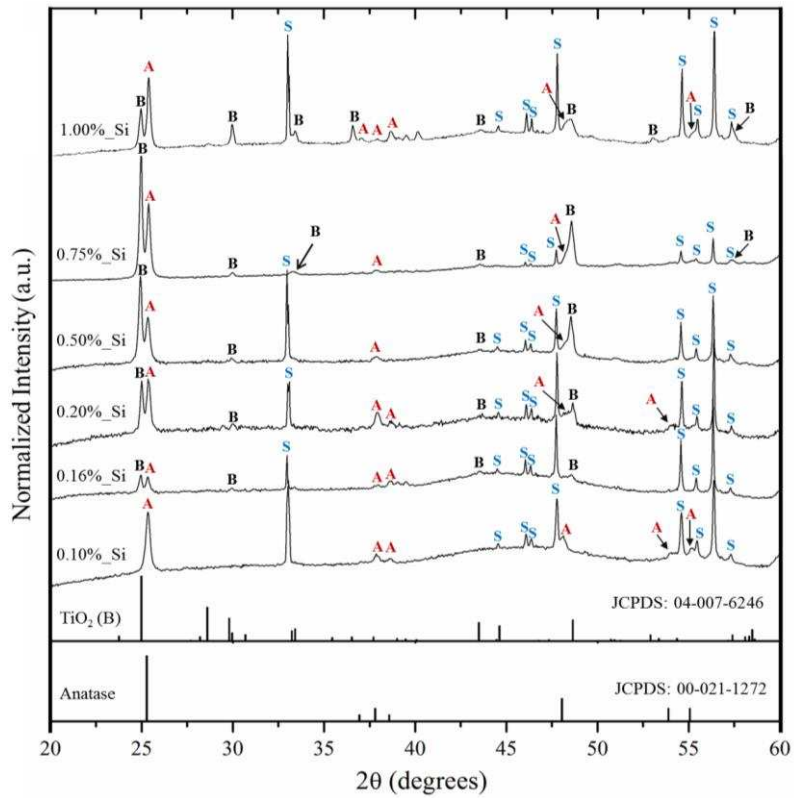


Fig. 15 XRD patterns of TiO₂ thin films deposited onto Si wafer substrates pre-coated with a very thin sodium-containing layer by spraying different concentrations of sodium ethoxide/ethanol solution; A, B and S refer to the TiO₂ Anatase phase, TiO₂(B) phase and Si wafer substrate respectively.

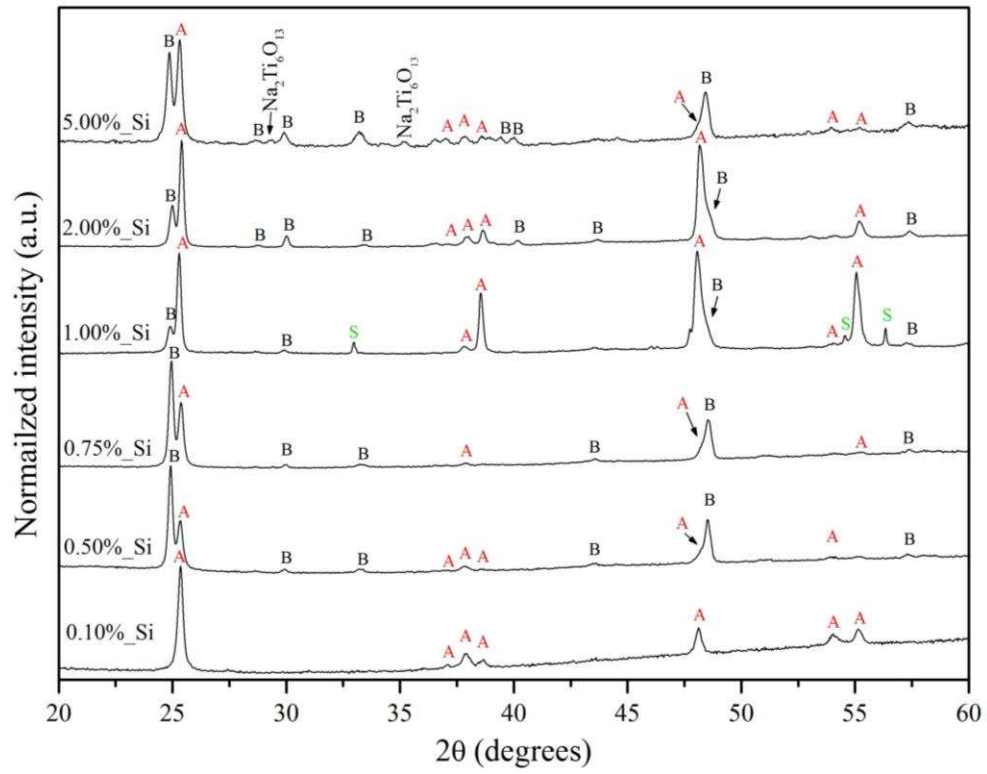


Fig. 16 Off axis XRD patterns of TiO₂ thin film samples showing the peaks due to the TiO₂ phase without interference from the silicon wafer substrate.

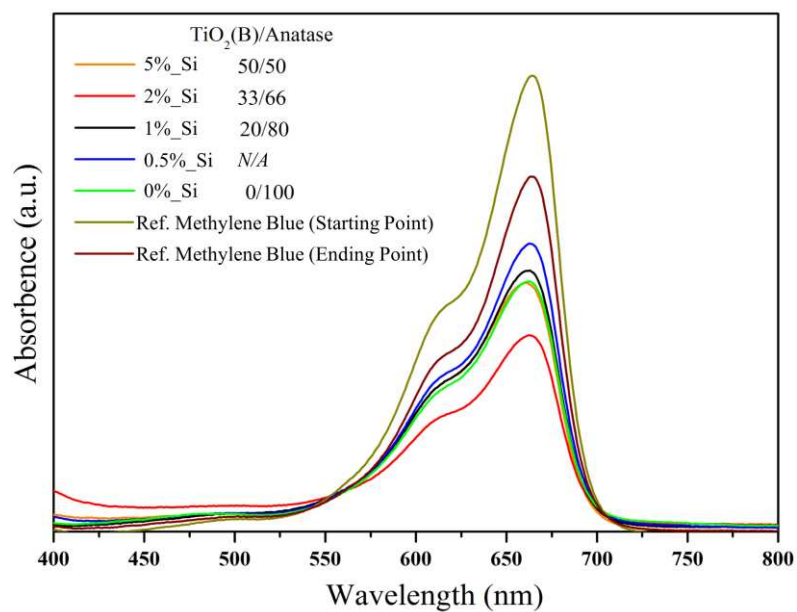


Fig. 17 UV-Vis spectra of methylene blue solutions after UV irradiation for 6 hr

Table 2. Comparison of methylene blue decolourization for 5 different mixed titania phase samples. Results have been normalised to a catalyst-free test.

Samples	%Phase composition		Crystallite size (nm)		% decolourization.#
	TiO ₂ (B)	Ana-tase	TiO ₂ (B)	Ana-tase	
0%_Si	-	100		31.4	23.2
0.5%_Si	62.2	37.8	36.2	30.0	14.8
1%_Si	20.7	79.3	28.0	36.8	20.9
2%_Si	29.4	70.6	28.9	37.5	34.9
5%_Si	47.2	52.8	28.2	29.5	23.9
Catalyst free					0.00

*The mole ratio of TiO₂(B) to anatase phase was estimated from the intensity ratio of the peaks at 24.98° and 25.28° of TiO₂(B) and anatase phases respectively – see text.

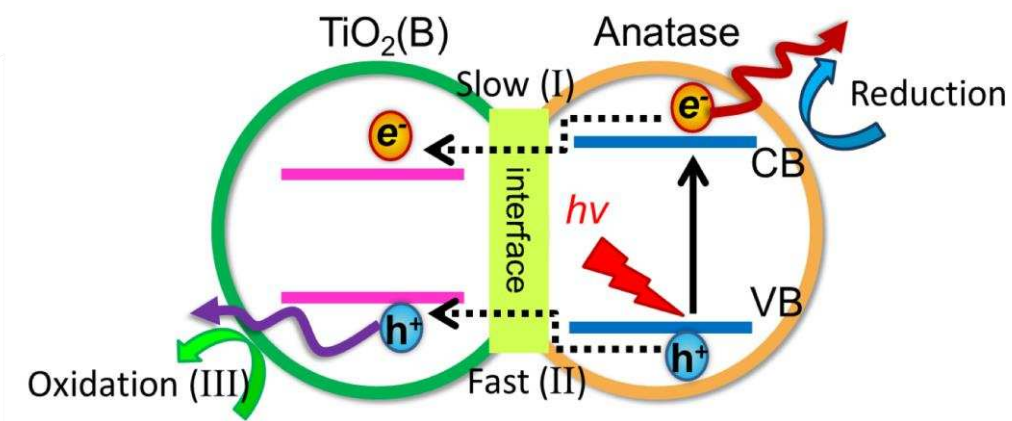


Fig. 18 Schematic description of the charge transfer processes and energy band structures for the mixed phases $\text{TiO}_2(\text{B})$ and anatase^{13,14}

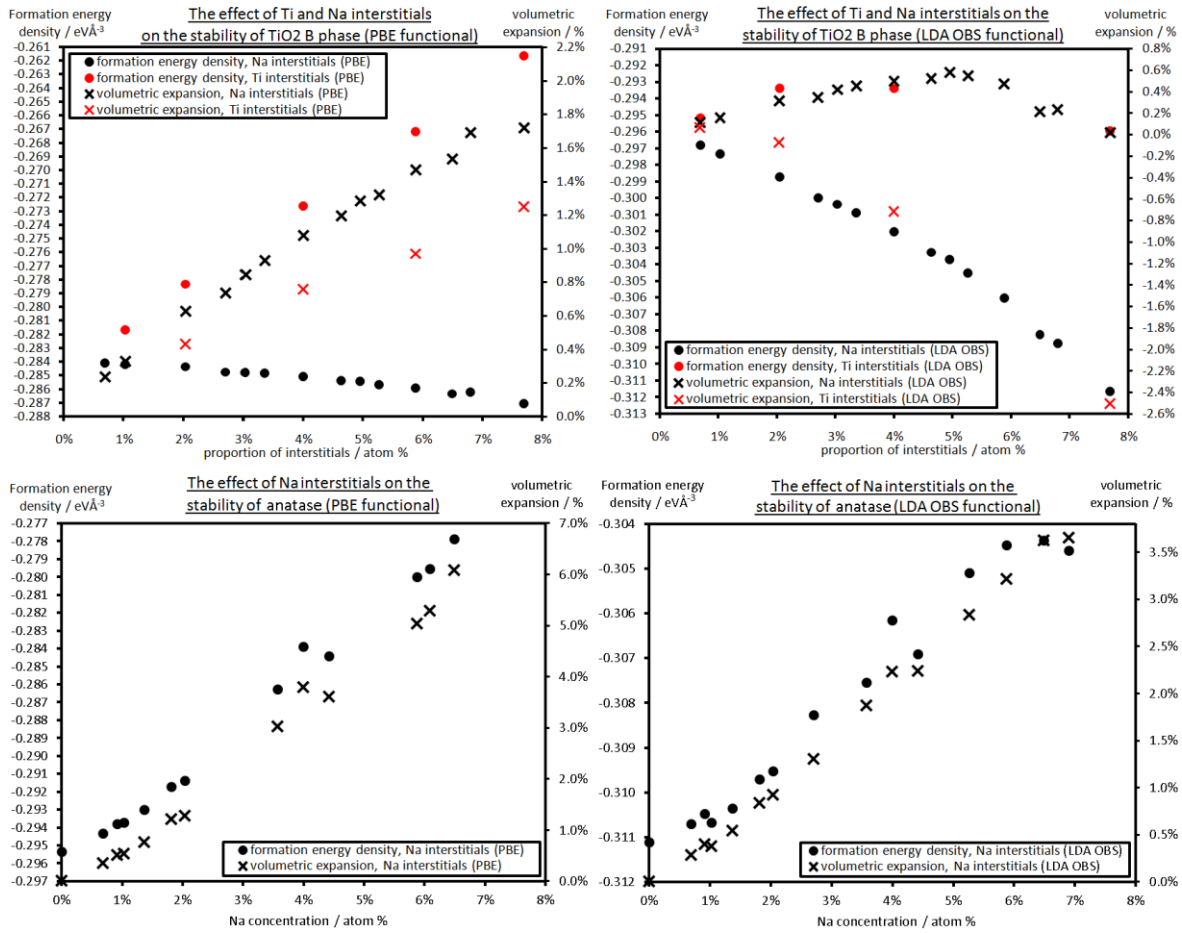


Fig. 19 The changes to total formation energy per unit volume with increasing Na concentration in various volume-relaxed anatase and B phase supercells. *Upper panels:* B phase supercells are seen to expand slightly but decrease in formation energy with increasing Na concentration. The two functionals disagree on the effect of Ti interstitials on B phase, which are predicted to either cause expansion and destabilisation (PBE) or contraction and no overall stabilisation (LDA OBS). *Lower panels:* Na clearly uses anatase to expand and become less stable with increasing concentration.

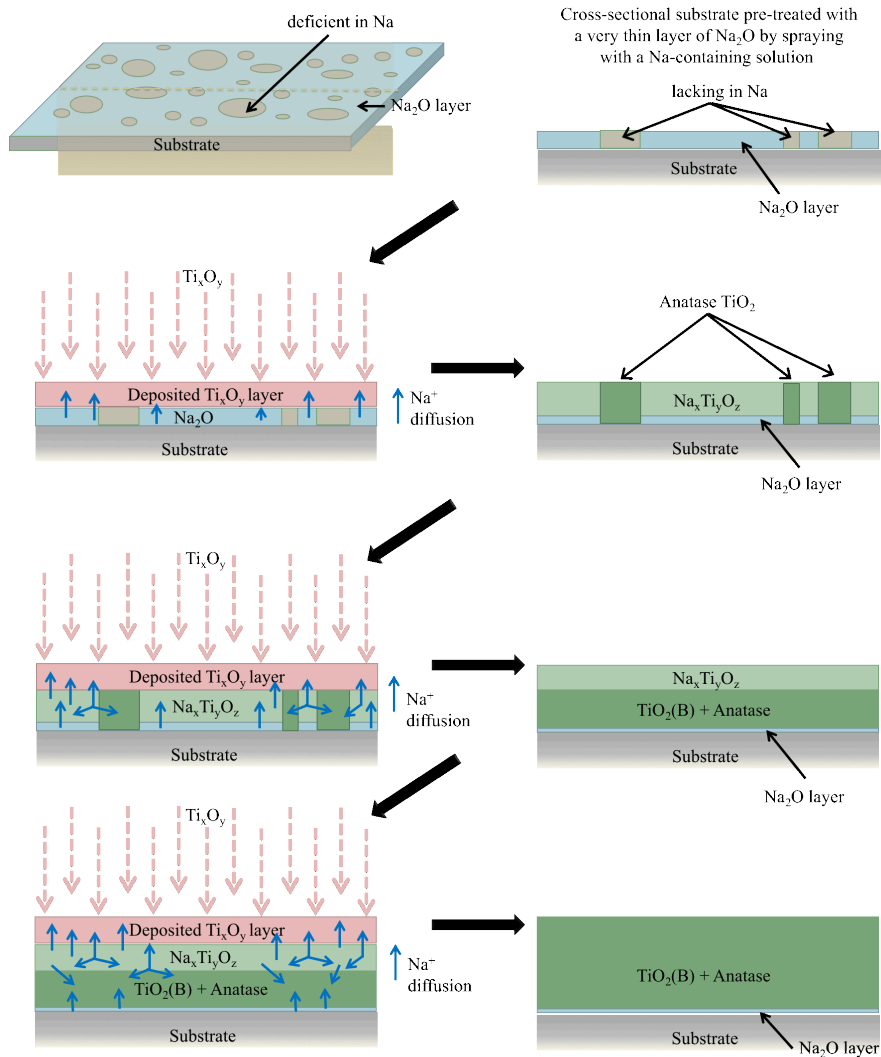


Fig. 20 Proposed mechanism for the synthesis of mixed phase $\text{TiO}_2(\text{B})/\text{anatase}$ thin films by LPCVD method onto substrate pre-treated with a very thin layer of Na-containing compound.

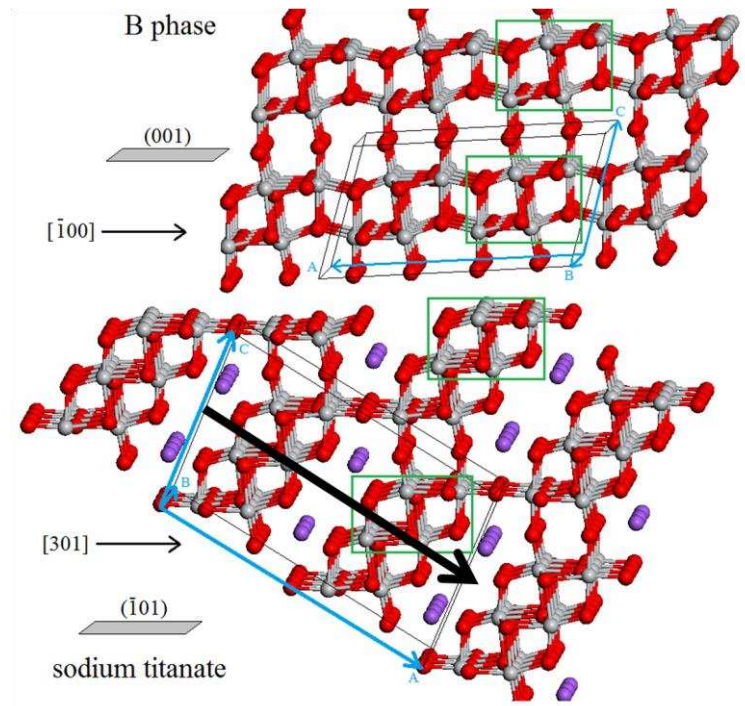


Fig. 21 The crystalline structures of Na₂Ti₆O₁₃ and TiO₂(B), showing the inter-conversion of Na₂Ti₆O₁₃ and TiO₂(B) by crystallographic shear (arrowed) of the titanate plane.